JM PAPERS

Revisiting the modelling framework for the unresolved scalar variance

Z. Nikolaou[1],†, P. Domingo[1] and L. Vervisch[1]

[1]CORIA-CNRS, Normandie Université, INSA de Rouen Normandie, 685 Av. de l'Université, 76800 Saint-Étienne-du-Rouvray, France

The unresolved scalar variance in large-eddy simulations of turbulent flows is a fundamental physical and modelling parameter. Despite its importance, relatively few algebraic models have been developed for this important variable with the most prominent models to date being the classic scale-similarity and gradient models. In this work a new generalized modelling framework based on reconstruction has been developed, which in contrast to classic modelling approaches allows the construction of base static variance models of arbitrary accuracy. It is demonstrated that higher-order reconstructions naturally lead to base static variance models of increased accuracy, and that the classic scale-similarity and gradient models are subsets of more general and higher-order models. The classic scale-similarity assumption for developing dynamic models is also revisited, and it is demonstrated that this can essentially be reinterpreted as a two-level reconstruction approach. Based on this result, a new general methodology is proposed that allows the construction of dynamic models for any given base static model, and a corresponding general reconstruction operator, algebraic or iterative. Consequently, improved static and dynamic models for the scalar variance are developed. The newly developed models are then thoroughly tested *a priori* using two high-fidelity direct numerical simulation databases corresponding to two substantially different flame and flow configurations, and are shown to outperform classic algebraic models for the variance.

Key words: computational methods, turbulent reacting flows, combustion

1. Introduction

The unresolved variance of a scalar ϕ is defined as

$$\sigma^2(\phi; \Delta) = \widetilde{\phi^2} - \tilde{\phi}\tilde{\phi}, \qquad (1.1)$$

† Email address for correspondence: zacharias.nikolaou@insa-rouen.fr

where $\tilde{\phi} = \overline{\rho\phi}/\bar{\rho}$ denotes standard Favre filtering using a filter G with a characteristic length scale $\Delta > 0$. In numerical simulations the scalar variance returns information on the level of resolution of the scalar field by the mesh, and provides a direct measure of the energy contained in the unresolved scalar fluctuations. The mechanisms of production/decay of the variance both for reactive and non-reactive scalars due to turbulent micro-mixing have been at the core of model development since the early days (Moss & Bray 1977; Dopazo 1979). The companion of the scalar variance is the scalar dissipation rate (Borghi 1988; Bilger, Saetran & Krishnamoorthy 1991; Bray 1996; Peters 2000; Veynante & Vervisch 2002; Pantano, Sarkar & Williams 2003) that calibrates the decay rate of the scalar fluctuations much like turbulent dissipation is the companion of the turbulent kinetic energy in the popular two-equation approach to turbulence modelling (Jones & Launder 1972). Therefore, the scalar variance and the scalar dissipation rate are among the fundamental ingredients of turbulent reactive flow modelling providing valuable information that can be used to infer the shape of the subgrid-scale (SGS) probability density function (p.d.f.) of the scalar (progress variable/mixture fraction). The concept of using a presumed p.d.f. for the SGS scalar p.d.f. was then introduced to average the response versus equivalence ratio (or mixture fraction) of reactive–diffusive layers under thermochemical equilibrium (Lockwood & Naguib 1975). This opened up many perspectives for combustion modelling using structural flame approaches in which the conditional response of the flame structure versus a given set of control parameters (mixture fraction, progress of reaction, scalar dissipation rate etc.) is averaged from the presumed p.d.f. Considering the asymptotic bimodal limit for the progress-variable p.d.f., the Bray–Moss–Libby theory was developed in which the scalar variance was key for investigating turbulent flame dynamics (Bray & Moss 1977; Bray, Libby & Moss 1985). These concepts were later extended to large-eddy simulation (LES) for predicting the distribution of chemical species including finite rate chemistry effects (Jimenez *et al.* 1997; Pierce & Moin 2004; Domingo, Vervisch & Veynante 2008; Lecocq *et al.* 2011; Nambully *et al.* 2014; Mesquita, Mastorakos & Zedda 2023). Therefore, accurate estimates of the scalar variance are required at various levels in the simulation of turbulent combustion, but also more generally in reactive flow modelling (Fox 2003).

Classic models for the scalar variance in LES can roughly be divided into two distinct categories: transport-equation-based models (Jimenez *et al.* 2001; Pera *et al.* 2006; Kolla *et al.* 2009; Keil, Klein & Chakraborty 2021) and algebraic models (Cook & Riley 1994; Girimaji & Zhou 1995; Pierce & Moin 1998, 2004; Balarac, Pitsch & Raman 2008). The consensus in the literature is that models based on a transport equation explicitly include the effects of reaction and transport. Such models however require a secondary modelling layer in order to close a number of unresolved terms that appear in the transport equation for the scalar variance. These include models for the scalar fluxes, unresolved source terms and a model for the scalar dissipation rate (Bilger *et al.* 1991; Kolla *et al.* 2009; Keil *et al.* 2021). Modelling all of these terms introduces further physical assumptions, additional levels of complexity, but also uncertainty with regards to the exact effects of each submodel's parameters on the evolution of the variance transport equation. In fact, quantifying the effects of numerical dissipation and model uncertainty on the evolution of the transport equation is a daunting task. Algebraic models on the other hand are computationally less expensive and straightforward to implement in LES. Notable examples include the scale-similarity model by Cook and Riley (Cook & Riley 1994) first proposed more than two decades ago, but also gradient-based models (Girimaji & Zhou 1995; Pierce & Moin 1998). Even though algebraic models do not explicitly account for reaction/transport, such effects may still in principle be modelled implicitly.

For instance, the classic dynamic model by Pierce & Moin (1998) originally developed for a passive scalar (by employing equilibrium assumptions) may still in principle incorporate the effects of reaction since reaction itself is a source of scalar gradients in the flow. Therefore, it is not surprising that gradient-based models have been used to successfully model the progress-variable variance in LES of turbulent premixed flames with overall good results (Vreman *et al.* 2008; Vreman, Bastiaans & Geurts 2009*a*; Vreman *et al.* 2009*b*; Mukhopadhyay, van Oijen & de Goey 2015). Nevertheless, even the development of algebraic models requires the introduction of a number of limiting assumptions/hypotheses that may not always be valid or well justified. Consequently, both of the above modelling approaches do not lead to a general and consistent modelling framework whereby models of arbitrary accuracy can readily be developed.

An alternative modelling framework with the potential to address the above issues is based on the concept of reconstruction/deconvolution. Reconstruction methods aim to recover quantitatively accurate estimates of the unfiltered fields ϕ^* from their filtered counterparts $\tilde{\phi}$ on the LES mesh. These reconstructions may then be used to estimate unresolved variables (scalar fluxes, Reynolds stresses, etc.) by explicit filtering. Probably the first successful implementation of reconstruction-modelling methods in LES dates to the works of Stolz and Adams who successfully simulated decaying homogeneous turbulence (Stolz & Adams 1999), boundary-layer flows (Stolz & Adams 2001) and flows with shocks (Adams & Stolz 2002). This LES modelling approach called approximate deconvolution modelling (ADM) consisted of a filtering step, followed by reconstruction and regularisation steps. In later works by Mathew *et al.* (2003) and Mathew, Foysi & Friedrich (2006), ADM was shown to be equivalent to using a single filtering step using a composite filter. Since then, many non-reacting LES studies have also employed reconstruction-modelling approaches (Schlatter, Stolz & Kleiser 2004; Loginov, Adams & Zheltovodov 2006; Boguslawski *et al.* 2021). In reacting flows, reconstruction-based models have been successfully applied probably first by Mathew (2002), and in a number of later studies (Domingo & Vervisch 2015; Wang & Ihme 2019; Domingo *et al.* 2020; Datta, Mathew & Hemchandra 2022). In the majority of these studies, approximate reconstruction methods were employed while in more recent *a priori* studies iterative and constrained reconstruction algorithms were developed. Such iterative algorithms were used to successfully model a variety of different unresolved terms in the LES transport equations including the scalar fluxes, and the Reynolds stresses (Domingo & Vervisch 2017; Wang & Ihme 2017; Nikolaou & Vervisch 2018; Nikolaou, Vervisch & Cant 2018; Nikolaou, Minamoto & Vervisch 2019). Reconstruction-modelling methods use information from the resolved scales in LES without invoking explicit assumptions on the underlying flow field and reaction mode. Even though in principle reconstruction cannot recover scales below the LES mesh, SGS effects can still be incorporated in a variety of approaches. For instance, Stolz & Adams (2001) added an additional relaxation term to the velocity transport equation proportional to the difference between the filtered and filtered-reconstructed velocity components $(\bar{u}_i - \overline{u_i^*})$. Wang & Ihme (2019) combined reconstruction with interpolation on a finer grid in an effort to enrich the information provided by the resolved scales on the LES mesh while Gullbrand & Chow (2003) employed mixed models. In yet another approach, Bull & Jameson (2016) assumed SGS dissipation to be sufficiently provided by the numerical scheme while reconstruction modelling was employed only for the unresolved LES scales. This modelling approach was applied to LES of turbulent channel flow, and improved the predictions over LES using the classic Smagorinsky model. In more recent works, data-based methods employing super-resolution reconstruction have also been considered (Fukami, Fukagata & Taira

2020; Kim *et al.* 2021). Therefore, the evidence in the literature seems to suggest that reconstruction modelling is a natural framework for modelling SGS effects as well.

With regards to modelling the scalar variance, a successful modelling framework based on iterative and constrained reconstruction was proposed and tested *a priori* by Nikolaou & Vervisch (2018). This framework provided quantitatively accurate predictions of the variance at a modest computational cost. Nevertheless, iterative reconstruction can be computationally expensive to apply in realistic-geometry LES. Data-based methods on the other hand (Maulik & San 2017; Nikolaou & Vervisch 2018) require high-quality and relatively large amounts of data. In addition, their computational efficiency depends strongly on the structure (number of layers, number of neurons) of the network, and there exist in fact bounds above which a neural network will always underperform (more floating-point operations) in comparison to using a simple tabulation approach (Nikolaou, Vervisch & Domingo 2022). One solution to this problem is to use approximate reconstruction operators derived from truncated Taylor-series expansions of the inverse filter operator. Such operators are computationally efficient, and lead to relatively simple analytic expressions that can be used to derive simple algebraic models with the deconvolution truncation order determining the model accuracy. Such approximate reconstruction methods have been considered before for modelling the scalar variance, for instance, by Balarac *et al.* (2008) and Knudsen, Kim & Pitsch (2010). Another approach that was recently proposed by Nikolaou, Vervisch & Domingo (2023) is to use inverse explicit discrete filters derived by solving an optimisation problem. This approach avoids the need to iterate as in most reconstruction algorithms and, as a result, reduces the reconstruction time by orders of magnitude (Nikolaou *et al.* 2023). Irrespective however of the reconstruction operator used (approximate, inverse filter, iterative), there does not appear to exist a structured and general reconstruction-based methodology for model development. For instance, it is unclear how the reconstructed fields should be employed, what conditions must be satisfied for the model to be physically realisable and how SGS effects can be incorporated in a general reconstruction-based model. The aim of this work is to address these issues by developing a general modelling framework based on reconstruction.

We begin in § 2 by discussing the most important properties of the scalar variance. In § 3, approximate reconstruction operators based on truncated Taylor-series expansions are derived. These operators are used to derive static models all the while maintaining compatibility with lower reconstruction-order models, but also with classic models in the literature. In § 4 a brief overview of the procedure for developing discrete inverse filters is presented, and in § 5 the classic dynamic models are revisited, and the dynamic procedure is reinterpreted in the context of reconstruction-based modelling. Finally, in § 6 the developed models are tested *a priori* using direct numerical simulation (DNS) data.

2. Variance properties

It is straightforward to show that the variance has the following properties:

$$\text{(i)} \quad \lim_{\Delta \to 0} \sigma^2(\phi; \Delta) = 0. \tag{2.1}$$

For *a*, *b* constant,

$$\text{(ii)} \quad \sigma^2(a\phi + b; \Delta) = a^2 \sigma^2(\phi; \Delta). \tag{2.2}$$

Provided the filter $G \geq 0$ and $\phi \in [0, 1]$,

$$\text{(iii)} \quad 0 \leq \sigma^2(\phi; \Delta) \leq \tilde{\phi}(1 - \tilde{\phi}) \leq \frac{1}{4}, \tag{2.3}$$

which we now prove formally. We begin from the definition of the filtering operation in a single dimension,

$$\bar{\phi}(x, t) = \int_{-\infty}^{\infty} G(x - s)\phi(s, t)\,\mathrm{d}s, \tag{2.4}$$

where $G(s) \geq 0$, $G(-s) = G(s)$ (symmetric) and $\int_{-\infty}^{\infty} G(x)\,\mathrm{d}x = 1$, which ensures that constant scalars are unaffected by the filtering (consistency condition). It is important to note at this point that we assume Δ to be constant, and that the computational mesh is homogeneous. In addition, a Cartesian coordinate system will be used throughout the analysis that follows. Since three-dimensional (3-D) filters are typically constructed using products of one-dimensional (1-D) filters, i.e. $G(x) = G(x)G(y)G(z)$, and filtering is conducted using dimensional splitting, it is sufficient to derive the variance bounds in the 1-D case. Favre-filtered variables are defined as usual, $\tilde{\phi}(x, t) = \overline{\rho(x, t)\phi(x, t)}/\bar{\rho}(x, t)$, and the equivalent Favre-filtering operation is

$$\tilde{\phi}(x, t) = \int_{-\infty}^{\infty} \tilde{G}(s; x, t)\phi(x - s, t)\,\mathrm{d}s, \tag{2.5}$$

where $\tilde{G}(s; x, t) = G(s)\rho(x - s, t)/\bar{\rho}(x, t)$ is the corresponding Favre filter. Clearly, $\tilde{G} \geq 0$ for any realisable (positive) value of the density, $\int_{-\infty}^{\infty} \tilde{G}(s; x, t)\,\mathrm{d}s = 1$ for all $x, t \in \mathbb{R}$, and for constant-density flows, $\tilde{G} = G$. The lower bound for the variance can be derived by making use of the Cauchy–Schwarz inequality that bounds from above the product $\tilde{\phi}\tilde{\phi}$,

$$\begin{aligned}
\tilde{\phi}(x, t)\tilde{\phi}(x, t) &= \left(\int_{-\infty}^{\infty} \tilde{G}(s; x, t)\phi(x - s, t)\,\mathrm{d}s \right)^2 \\
&= \left(\int_{-\infty}^{\infty} \sqrt{\tilde{G}(s; x, t)}\sqrt{\tilde{G}(s; x, t)}\phi(x - s, t)\,\mathrm{d}s \right)^2 \\
&\leq \underbrace{\int_{-\infty}^{\infty} \tilde{G}(s; x, t)\,\mathrm{d}s}_{1} \cdot \int_{-\infty}^{\infty} \tilde{G}(s; x, t)\phi^2(x - s, t)\,\mathrm{d}s \\
&= \widetilde{\phi^2}(x, t).
\end{aligned} \tag{2.6}$$

Now suppose $\phi(x, t)$ is a bounded scalar specifically $\phi \in [0, 1]$. Such scalars of interest may, for instance, be the progress variable in premixed flames, the mixture fraction in non-premixed flames, the mass fraction, etc. Since $\phi \in [0, 1]$, $\phi^2 \leq \phi$, hence, $\widetilde{\phi^2} \leq \tilde{\phi}$ provided $\tilde{G}(s; x, t) \geq 0$. Therefore, we have overall $\tilde{\phi}\tilde{\phi} \leq \widetilde{\phi^2} \leq \tilde{\phi}$ and $0 \leq \sigma^2 = \widetilde{\phi^2} - \tilde{\phi}\tilde{\phi} \leq \tilde{\phi}(1 - \tilde{\phi}) \leq \frac{1}{4}$.

It is important to note that, for positive filters, if $\phi \in [0, 1]$ then $\tilde{\phi} \in [0, 1]$ as well irrespective of the distribution of ϕ, but this is not necessarily the case for non-positive filters. A short proof of this is given in Appendix A, and as we will see later on this has some important modelling consequences. In principle, properties (i)–(iii) must be satisfied by any variance model.

Filter	$G(x)$	$\hat{G}(k)$	M_{2r}	$a_2 = M_2/2$	$a_2' = M_2'/2$
Gaussian	$\dfrac{\sqrt{6}}{\Delta\sqrt{\pi}}\exp\left(-\dfrac{6x^2}{\Delta^2}\right)$	$\exp\left(\dfrac{-\Delta^2 k^2}{24}\right)$	$\dfrac{(2r)!}{r!}\left(\dfrac{\Delta}{2\sqrt{6}}\right)^{2r}$	$\Delta^2/24$	$\hat{\Delta}^2/24$
Helmholtz	$\dfrac{1}{2\Delta}e^{-|x|/\Delta}$	$\dfrac{1}{1+\Delta^2 k^2}$	$(2r)!\Delta^{2r}$	Δ^2	$\hat{\Delta}^2$

Table 1. Common explicit positive filters with their transfer functions and even moments M_{2r}.

3. Approximate reconstruction using truncated Taylor series

Starting from the 3-D filtering operation that, for convenience, we now write as (using the filter symmetry condition)

$$\bar{\phi}(x) = \int_{-\infty}^{\infty} G(r)\phi(x+r)\,\mathrm{d}r \tag{3.1}$$

and expanding $\phi(x+r)$ in Taylor series around $r = x$, it is straightforward to show after some algebraic manipulation that (Nikolaou *et al.* 2023)

$$\bar{\phi}(x) = \phi(x) + a_2 \nabla \cdot \nabla \phi + O(\Delta^4) = \phi(x) + a_2 \frac{\partial}{\partial x_i}\left(\frac{\partial \phi}{\partial x_i}\right) + O(\Delta^4), \tag{3.2}$$

where $a_2 = M_2/2$ is half the filter's second moment. For a Gaussian filter, $a_2 = \Delta^2/24$ while for a Helmholtz filter, $a_2 = \Delta^2$; table 1 lists two of the most popular filters (Gaussian/Helmholtz) along with their transfer functions, moments and other important parameters. Taking the Fourier transform (here $\wedge$ denotes Fourier transform) of the above expansion we obtain

$$\hat{\bar{\phi}}(k) = \hat{\phi}(k) + a_2(jk)(jk)\hat{\phi}(k) + O(k^4), \tag{3.3}$$

which we can invert approximately to obtain

$$\hat{\phi}(k) = \hat{\bar{\phi}}(k)\left(1 - a_2 kk + O(k^4)\right)^{-1} = \hat{\bar{\phi}}(k) + a_2\hat{\bar{\phi}}(k)kk + O(k^4). \tag{3.4}$$

The above equation is an approximation of the Fourier transform of the inverse filter – an alternative approach to obtain this for a specific filter is to use the exact transform of the inverse filter used. For a Gaussian filter, for instance, $\hat{G}^{-1} = e^{\Delta^2 k^2/24}$ that can be expanded in Taylor series resulting in the same expression as above (Balarac *et al.* 2008). Taking an inverse Fourier transform of the above we obtain an approximation ϕ^* of the original field ϕ,

$$\phi^*(x) = \bar{\phi}(x) - a_2 \nabla \cdot \nabla \bar{\phi}(x) + O(\Delta^4). \tag{3.5}$$

For a forward filter having a filter width Δ, the above equation is an approximation of the unfiltered field with a truncation order of $O(\Delta^4)$. As $\Delta \to 0$, $a_2 \to 0$ while $\bar{\phi}(x) \to \phi(x)$, hence, $\phi^*(x) \to \phi(x)$. The above approximation holds for any filter, and higher-order approximations/reconstructions can be obtained by including higher-order derivatives (Leonard 1997; Carati, Winckelmans & Jeanmart 2001); however, such expressions become substantially more complex for deriving (simple) algebraic models. The reconstruction operation in (3.5) can also be written in terms of a reconstruction operator $R_\Delta = (I - a_2\nabla^2)$ acting on the filtered scalar ϕ, i.e. $R_\Delta[\bar{\phi}]$. This notation will prove useful in the sections that follow.

3.1. *Constant-density flows*

The approximate reconstruction operator in (3.5) opens up a number of possibilities for modelling the scalar variance. We begin with constant-density flows where $\sigma^2 = \overline{\phi^2} - \bar{\phi}\bar{\phi}$. One option would be to model the variance using $\overline{\phi^{*2}} - \bar{\phi}\bar{\phi}$ since $\overline{\phi^2}$ is the unresolved part. However, this approach involves two distinct fields (ϕ, ϕ^*) and properties (ii)–(iii) of § 2 may not always be satisfied. An alternative option is to use

$$\sigma^2 = \overline{\phi^{*2}} - \overline{\phi^*}\,\overline{\phi^*}, \tag{3.6}$$

where ϕ^* is the reconstructed scalar on the LES mesh. Clearly, as $\Delta \to 0$, the filter must tend to a δ function, and property (i) is satisfied. Property (ii) is always satisfied inherently – this follows from the linearity of the filtering operation and the filter's consistency condition. With regards to property (iii), provided $\phi^* \in [0, 1]$ then, as shown in Appendix A, $\overline{\phi^*} \in [0, 1]$ as well. As a result, the predictions of the above model will be bounded in a similar manner as the actual variance specifically in the region $[0, \overline{\phi^*}(1 - \overline{\phi^*})]$. For a perfect reconstruction, $\phi^* \to \phi$, and the model bounds approach the actual variance bounds. For an imperfect reconstruction, the model bounds may not necessarily coincide with the actual variance bounds but guarantee that the theoretical upper bound of 1/4 is never exceeded. This is in contrast with models of the gradient type that are not intrinsically bounded, and whose upper bound depends solely on the magnitude of the scalar gradient.

With the above modelling approach, and an $O(\Delta^2)$ approximation of ϕ, i.e. $\phi^* = \bar{\phi} + O(\Delta^2)$, we obtain the model

$$\sigma^2(\phi) = \overline{\bar{\phi}\bar{\phi}} - \bar{\bar{\phi}}\bar{\bar{\phi}} + O(\Delta^2), \tag{3.7}$$

which is essentially the scale-similarity model of Bardina, Ferzinger & Reynolds (1980) applied to a scalar. The bounds of this model are $[0, \bar{\bar{\phi}}(1 - \bar{\bar{\phi}})]$. We will refer to this model as the SM2 model for constant-density flows. For an $O(\Delta^4)$ approximation on the other hand, i.e. $\phi^* = \bar{\phi} - a_2\nabla^2\bar{\phi}$, we obtain

$$\begin{aligned}
\sigma^2 &= \overline{(\bar{\phi} - a_2\nabla^2\bar{\phi})^2} - \overline{(\bar{\phi} - a_2\nabla^2\bar{\phi})} \cdot \overline{(\bar{\phi} - a_2\nabla^2\bar{\phi})} + O(\Delta^4) \\
&= \underbrace{\overline{\bar{\phi}\bar{\phi}} - \bar{\bar{\phi}}\bar{\bar{\phi}}}_{\text{SM2}} + 2a_2\left(\bar{\bar{\phi}}\nabla^2\bar{\bar{\phi}} - \overline{\bar{\phi}\nabla^2\bar{\phi}}\right) + O(\Delta^4).
\end{aligned} \tag{3.8}$$

The above model is composed of the SM2 model term in (3.7) ensuring compatibility, and an additional correction term that arises from the higher-order reconstruction terms retained in the expression for ϕ^*. We will refer to the above model as the SM4 model. Following this modelling procedure it is clear that one may develop higher-order models by retaining higher-order terms in the Taylor-series expansion all the while ensuring backwards compatibility with lower-order models. In contrast with the SM2 model however, the variance bounds may not be satisfied for the SM4 model since the $O(\Delta^4)$ reconstruction that involves gradients of $\tilde{\phi}$ may cause ϕ^* to lie outside its physical limits and, as a result, so will the variance predictions. A remedy to this problem will be presented in the sections that follow. For now, we focus our attention on the SM4 model. If we further expand all the double-filtering operations in (3.8) in Taylor series and truncate

$$\Delta \qquad\qquad \hat{\Delta}$$

$$\tilde{u} = \overline{\rho u}/\bar{\rho} \qquad\qquad \check{u} = \widehat{\bar{\rho} u}/\hat{\bar{\rho}}$$

$$\widetilde{u^*} = \overline{\rho^* u^*}/\overline{\rho^*} \qquad\qquad \check{u}^* = \widehat{\overline{\rho^* u^*}}/\widehat{\overline{\rho^*}}$$

$$\check{u} = \overline{\bar{\rho} u}/\bar{\bar{\rho}} \qquad\qquad \hat{u} = \widehat{\hat{\bar{\rho}} u}/\hat{\hat{\bar{\rho}}}$$

$$u^* = R_\Delta[\bar{u}] \qquad\qquad u_L^* = R_{\hat{\Delta}}[\hat{\bar{u}}]$$

Table 2. Operations involving the normal filter Δ and the test filter $\hat{\Delta}$.

these to $O(\Delta^4)$, we obtain

$$\sigma^2 = \overline{\bar{\phi}\bar{\phi}} - \bar{\bar{\phi}}\bar{\bar{\phi}} + 2a_2\left(\bar{\bar{\phi}}\nabla^2\bar{\bar{\phi}} - \overline{\bar{\phi}\nabla^2\bar{\phi}}\right)$$

$$= \bar{\phi}\bar{\phi} + a_2\nabla^2\bar{\phi}\bar{\phi} + O(\Delta^4) - \left(\bar{\phi} + a_2\nabla^2\bar{\phi} + O(\Delta^4)\right)^2 + \left(\bar{\phi}\nabla^2\bar{\phi} - \bar{\phi}\nabla^2\bar{\phi} + O(\Delta^4)\right)$$

$$= a_2\nabla^2\bar{\phi}\bar{\phi} - 2a_2\bar{\phi}\nabla^2\bar{\phi} + O(\Delta^4)$$

$$= 2a_2\frac{\partial\bar{\phi}}{\partial x_i}\frac{\partial\bar{\phi}}{\partial x_i} + O(\Delta^4). \tag{3.9}$$

The above is none other than the gradient model but having a well-defined model parameter given by $2a_2 = M_2$ that, for a Gaussian filter, is $\Delta^2/12$ – a similar expression was derived for the Reynolds stresses by Clark, Ferzinger & Reynolds (1979). Therefore, based on the above procedure, we see that the gradient model is a subset model of the more general scale-similarity model in (3.8) (SM4).

3.2. *Variable-density flows*

For variable-density flows, the modelling procedure becomes somewhat more complicated but the key idea remains the same: we use approximate reconstructions $\rho^* = R_\Delta[\bar{\rho}]$ and $(\rho\phi)^* = R_\Delta[\overline{\rho\phi}]$ in order to obtain an expression for the variance. For variable-density flows, in the same spirit as for constant-density flows, we model the variance using

$$\sigma^2 = \frac{\overline{\rho^*\phi^*\phi^*}}{\overline{\rho^*}} - \left(\frac{\overline{\rho^*\phi^*}}{\overline{\rho^*}}\right)^2 = \widetilde{\phi^*\phi^*} - \widetilde{\phi^*}\widetilde{\phi^*}, \tag{3.10}$$

where $\phi^* = (\rho\phi)^*/\rho^*$; table 2 lists all the different operations/notations that will be used throughout the rest of the paper for clarity. The above model satisfies conditions (i) and (ii) always and provided $\phi^* \in [0, 1]$ the model bounds are $[0, \widetilde{\phi^*}(1 - \widetilde{\phi^*})]$. Therefore, as $\phi^* \to \phi$, the bounds approach the actual variance bounds. For an imperfect reconstruction on the other hand, these bounds ensure that the upper bound of 1/4 is never exceeded.

For an $O(\Delta^2)$ approximation, $\rho^* = \bar{\rho} + O(\Delta^2)$ and $(\rho\phi)^* = \overline{\rho\phi} + O(\Delta^2)$. Inserting these in (3.10) we obtain the equivalent SM2 model for variable-density flows:

$$\sigma^2 = \frac{\overline{\bar{\rho}\tilde{\phi}\tilde{\phi}}}{\bar{\bar{\rho}}} - \left(\frac{\overline{(\bar{\rho}\tilde{\phi})}}{\bar{\bar{\rho}}}\right)^2 = \left(\tilde{\phi}\tilde{\phi}\right)^{\check{}} - \check{\tilde{\phi}}\check{\tilde{\phi}}. \tag{3.11}$$

Here $\breve{\tilde{\phi}} = \overline{\bar{\rho}\tilde{\phi}}/\bar{\rho}$ (notation that is extended in the form $(\cdot)\breve{} = \overline{\bar{\rho}\cdot}/\bar{\rho}$ in (3.11)). The bounds of the above model are $[0, \breve{\tilde{\phi}}(1 - \breve{\tilde{\phi}})]$. Note that, for constant-density flows, $\breve{\tilde{\phi}} = \bar{\tilde{\phi}}$ and (3.11) reduces to (3.7) thus ensuring compatibility with the constant-density case. For an $O(\Delta^4)$ approximation, the reconstruction operator is given by

$$R_\Delta[\bar{u}] = \bar{u} - a_2 \nabla^2 \bar{u}; \tag{3.12}$$

therefore, $\rho^* = \bar{\rho} - a_2 \nabla^2 \bar{\rho} + O(\Delta^4)$, $(\rho\phi)^* = \overline{\rho\phi} - a_2 \nabla^2 \overline{\rho\phi} + O(\Delta^4)$, and it is straightforward to show after some algebraic manipulation that

$$\left(\frac{\overline{(\rho\phi)^*}}{\overline{\rho^*}}\right)^2 = \breve{\tilde{\phi}}\breve{\tilde{\phi}} + 2\frac{a_2}{\bar{\bar{\rho}}}\breve{\tilde{\phi}}\breve{\tilde{\phi}}\nabla^2\bar{\bar{\rho}} - 2\frac{a_2}{\bar{\bar{\rho}}}\breve{\tilde{\phi}}\nabla^2\overline{\bar{\rho}\tilde{\phi}} + O(\Delta^4) \tag{3.13}$$

and

$$
\begin{aligned}
(\rho\phi^2)^* &= \frac{(\rho\phi)^*(\rho\phi)^*}{\rho^*} \\
&= \frac{\left(\overline{\rho\phi} - a_2\nabla^2\overline{\rho\phi} + O(\Delta^4)\right)^2}{\bar{\rho} - a_2\nabla^2\bar{\rho} + O(\Delta^4)} \\
&= \frac{1}{\bar{\rho}}\left(\overline{\rho\phi}\cdot\overline{\rho\phi} - 2a_2\overline{\rho\phi}\nabla^2\overline{\rho\phi} + O(\Delta^4)\right)\left(1 - \frac{a_2}{\bar{\rho}}\nabla^2\bar{\rho} + O(\Delta^4)\right)^{-1} \\
&= \frac{1}{\bar{\rho}}\left(\overline{\rho\phi}\cdot\overline{\rho\phi} - 2a_2\overline{\rho\phi}\nabla^2\overline{\rho\phi} + O(\Delta^4)\right)\left(1 + \frac{a_2}{\bar{\rho}}\nabla^2\bar{\rho} + O(\Delta^4)\right) \\
&= \bar{\rho}\tilde{\phi}\tilde{\phi} + a_2\tilde{\phi}\tilde{\phi}\nabla^2\bar{\rho} - 2a_2\tilde{\phi}\nabla^2\overline{\bar{\rho}\tilde{\phi}} + O(\Delta^4),
\end{aligned} \tag{3.14}
$$

which constitutes an $O(\Delta^4)$ approximation of $\rho\phi^2$. Inserting the above in (3.10) we eventually obtain the equivalent SM4 model for variable-density flows:

$$\sigma^2 = \underbrace{\left(\tilde{\phi}\tilde{\phi}\right)\breve{} - \breve{\tilde{\phi}}\breve{\tilde{\phi}}}_{\text{SM2}} + \frac{2a_2}{\bar{\bar{\rho}}}\left(\breve{\tilde{\phi}}\nabla^2\overline{\bar{\rho}\tilde{\phi}} - \overline{\tilde{\phi}}\nabla^2\overline{\bar{\rho}\tilde{\phi}}\right) + \frac{a_2}{\bar{\bar{\rho}}}\left(\overline{\tilde{\phi}\tilde{\phi}\nabla^2\bar{\rho}} + \left(\tilde{\phi}\tilde{\phi}\right)\breve{}\nabla^2\bar{\bar{\rho}} - 2\breve{\tilde{\phi}}\breve{\tilde{\phi}}\nabla^2\bar{\bar{\rho}}\right). \tag{3.15}$$

The above model is composed of the scale-similarity term of the SM2 model in (3.11) augmented by two more correction terms. For constant-density flows, the entire third term in the parentheses disappears, in which case we recover (3.8). If we further expand all filtering operations up to $O(\Delta^4)$ it is straightforward to show that

$$\breve{\tilde{\phi}} = \tilde{\phi} + a_2\nabla^2\tilde{\phi} + \frac{2a_2}{\bar{\rho}}\frac{\partial\bar{\rho}}{\partial x_i}\frac{\partial\tilde{\phi}}{\partial x_i} + O(\Delta^4), \tag{3.16}$$

$$\breve{\tilde{\phi}}\breve{\tilde{\phi}} = \tilde{\phi}\tilde{\phi} + 2a_2\tilde{\phi}\nabla^2\tilde{\phi} + \frac{4a_2}{\bar{\rho}}\tilde{\phi}\frac{\partial\bar{\rho}}{\partial x_i}\frac{\partial\tilde{\phi}}{\partial x_i} + O(\Delta^4) \tag{3.17}$$

and

$$\left(\tilde{\phi}\tilde{\phi}\right)\breve{} = \tilde{\phi}\tilde{\phi} + 2a_2\tilde{\phi}\nabla^2\tilde{\phi} + 2a_2\frac{\partial\tilde{\phi}}{\partial x_i}\frac{\partial\tilde{\phi}}{\partial x_i} + \frac{4a_2}{\bar{\rho}}\tilde{\phi}\frac{\partial\bar{\rho}}{\partial x_i}\frac{\partial\tilde{\phi}}{\partial x_i} + O(\Delta^4). \tag{3.18}$$

Since the second and third terms in (3.15) already include a Δ^2 term in the parameter a_2 outside of the parentheses, all terms inside the parentheses must be expanded up to

$O(\Delta^2)$ only to keep the overall expansion order to $O(\Delta^4)$, i.e. $\check{\tilde{\phi}} = \tilde{\phi}$, $\bar{\bar{\rho}} = \bar{\rho}$, etc., causing them to vanish. As a result, after some algebraic manipulation the approximation of (3.15) eventually reduces to

$$\sigma^2 = 2a_2 \frac{\partial \tilde{\phi}}{\partial x_i} \frac{\partial \tilde{\phi}}{\partial x_i} + O(\Delta^4), \tag{3.19}$$

which is the gradient model for variable-density flows. Therefore, the gradient model is a subset model of the more general reconstruction-based SM4 model of (3.15). It is important to note that this derivation of the gradient model is based on a purely mathematical approach using approximate reconstruction operators. No explicit assumptions on the nature/structure of the scalar (passive, reactive) and/or the flow field were made in this process. This implies that the gradient model alone should in principle be sufficient to model both non-reactive and reactive scalars as evidenced by previous LES of turbulent premixed flames (Vreman *et al.* 2008, 2009*a*,*b*; Mukhopadhyay *et al.* 2015) that employed either the static or the dynamic gradient model.

3.3. *Post-reconstruction bounding*

For a general reconstruction operator R_Δ, (3.10) may not necessarily satisfy the variance bounds because $\phi^* = (\rho\phi)^*/\rho^*$ may not lie in the range [0, 1]. Possible reasons for this may include ρ^*, $(\rho\phi)^*$ lying outside their physical minimum/maximum limits because of approximate reconstruction, but also due to numerical errors. A straightforward remedy to this problem is to bound the reconstructed fields. Therefore, (3.10) is still employed, but using the bounded reconstructed fields instead such that $\phi^* \in [0, 1]$ by construction. Bounding serves two purposes: (i) that $\tilde{\phi}^* \in [0, 1]$, and (ii) that the bounds for (3.10) are $[0, \tilde{\phi}^*(1 - \tilde{\phi}^*)]$ always.

One approach to implement bounding is directly in the reconstruction operator R_Δ, i.e. use a constrained reconstruction algorithm, and such algorithms were employed in previous *a priori* (Wang & Ihme 2017; Nikolaou & Vervisch 2018) and *a posteriori* (Wang & Ihme 2019) studies. Constrained reconstruction guarantees that $\phi^* \in [0, 1]$, but is generally computationally more expensive than unconstrained reconstruction, and may also hinder the convergence of the deconvolution process. A computationally more efficient approach is to use post-reconstruction bounding. Provided the reconstruction operator is sufficiently accurate, post-reconstruction bounding helps to bound the minority of points lying outside their physical boundaries. A general approach for doing so is to use two levels of bounding: a physical one and a numerical one. For a general reconstruction operator R_Δ, physical bounding may be applied in a computationally efficient approach using

$$\rho^* = \max\left(\min\left(R_\Delta[\bar{\rho}], \rho_h\right), \rho_l\right), \tag{3.20}$$

$$(\rho\phi)^* = \max\left(\min\left(R_\Delta[\overline{\rho\phi}], (\rho\phi)_h\right), (\rho\phi)_l\right), \tag{3.21}$$

where the subscripts l, h denote the corresponding low and high values. Alternatively, a smoother function other than maxmin can also be employed. Physical bounding ensures that the reconstructed fields lie within their physical limits. For instance, in the case of premixed flames $\rho_l = \rho_p$ the density of the hot products, and $\rho_h = \rho_r$ the density of the cold reactants while $(\rho\phi)_l = 0$ and $(\rho\phi)_h = \rho_r$. Following physical bounding, numerical

bounding can also be applied directly on ϕ^* using

$$\phi^* = \max\left(\min\left((\rho\phi)^*/\rho^*, 1\right), 0\right), \tag{3.22}$$

which ensures that any numerical errors in evaluating ϕ^* from the physically bounded reconstructions do not cause it to exceed the limits [0, 1]. As we show later on, the above approach substantially improves the reconstructions, hence, the variance predictions. To illustrate the procedure, we consider an $O(\Delta^4)$ reconstruction operator, $R_\Delta = (I - a_2\nabla^2)$, in which case we have

$$\rho^* = \max\left(\min\left((I - a_2\nabla^2)[\bar{\rho}], \rho_h\right), \rho_l\right), \tag{3.23}$$

$$(\rho\phi)^* = \max\left(\min\left((I - a_2\nabla^2)[\overline{\rho\phi}], (\rho\phi)_h\right), (\rho\phi)_l\right). \tag{3.24}$$

Calculating ϕ^* using (3.22)–(3.24), and inserting all in (3.10) we obtain a scalar variance model bounded exactly in the range $[0, \widetilde{\phi}^*(1 - \widetilde{\phi}^*)]$ – we will refer to this particular model as AD4. Note however that the above procedure is general, and can be applied for any general reconstruction operator R_Δ that may well be based on any reconstruction algorithm.

4. Inverse filter reconstruction

Higher-order reconstruction operators R_Δ can be obtained using iterative algorithms such as van Cittert iterations (van Cittert 1931). A constrained version of this algorithm was introduced in previous work (Nikolaou & Vervisch 2018) where it was used to successfully model the progress-variable variance in turbulent premixed flames. In iterative algorithms the iteration count N determines the extent of reconstruction with higher N corresponding to higher-order reconstruction (larger wavenumbers are recovered). Compared with approximate reconstruction methods such as the one presented in the previous section, iterative methods have superior performance albeit at an increased computational cost that depends on N, the stencil size of the filter, but also the problem dimension – an expression quantifying this has been developed by Nikolaou *et al.* (2023). An alternative computationally efficient yet high-order reconstruction process recently proposed by Nikolaou *et al.* (2023) is based on the concept of inverse discrete filters. In this approach, the same way a discrete forward explicit filter is used to filter a signal, an inverse discrete explicit filter is applied on the filtered signal in order to recover a reconstruction estimate. This approach was demonstrated to be computationally more efficient (by orders of magnitude) than iterative reconstruction while maintaining the same level of accuracy (Nikolaou *et al.* 2023).

The procedure for obtaining an optimised inverse filter begins by first obtaining an optimised forward filter. We begin from the 1-D discrete and explicit filtering operation defined as

$$\bar{u}_i = G_d \circledast u_i = \sum_{l=-M}^{M} g_l u_{i+l}, \tag{4.1}$$

where M is the half-stencil size of the filter and g_l are the discrete filter coefficients for each point on the stencil (we will be dealing with symmetric filters). With a mesh spacing h, $x_i = ih$, $i \in [0, N_x - 1]$, the transfer function $\hat{G}_d$ of the above discrete filtering operation

is given by

$$\hat{G}_d(k_r) = \sum_{l=-M}^{M} g_l e^{jk_r hl} = g_0 + 2\sum_{l=1}^{M} g_l \cos(k_r hl), \tag{4.2}$$

where $k_r = 2\pi r/(N_x h)$. The coefficients g_l in (4.2) completely determine $\hat{G}_d$ that ideally should match $\hat{G}$ (the actual filter transfer function) for all $k_r h \in [0, \pi]$. Standard methods for obtaining the filter coefficients include Newton–Cotes rules, using filters derived from truncated Taylor expansions, etc. As discussed in Nikolaou *et al.* (2023), both of these approaches have some important drawbacks. For instance, filters based on Newton–Cotes rules generally have poorer responses at higher wavenumbers, and are not consistent ($\hat{G}_d(0) \neq 1$). Filters based on Taylor expansions on the other hand are consistent, but their predictive ability deteriorates above a threshold value of $\gamma = \Delta/h$. In addition, in both of these approaches there is no explicit error control. In order to circumvent such issues, but at the same time to automate the process for developing discrete filters, an optimisation procedure was proposed to obtain the coefficients g_l. The optimisation problem reads

$$\arg\min_{g_l} \left(\int_{kh=0}^{\pi} \left(\hat{G}_d(kh; g_l) - \hat{G}(kh; \gamma) \right)^2 d(kh) \right). \tag{4.3}$$

To ensure consistency ($\hat{G}_d(0) = 1$), the following constraint is applied:

$$g_0 + 2\sum_{l=1}^{M} g_l = 1. \tag{4.4}$$

To ensure $0 \le \hat{G}_d \le 1$ (positive transfer function), an additional constraint is introduced,

$$\hat{G}(\pi) \le g_0 + 2\sum_{l=1}^{M} g_l \cos(k_r hl) \le 1 \quad \text{for all } k_r h \in (0, \pi]. \tag{4.5}$$

The optimisation problem can be solved by providing the actual transfer function $\hat{G}$ and half-stencil size M, but can also be solved adaptively. In the adaptive version, which is the approach used here, $\hat{G}$ and the target optimisation error are provided. An error controller then adjusts M until the target optimisation error is obtained. Once the optimised 1-D filter coefficients are obtained, for the 3-D case the filtering operation is calculated using dimensional splitting, i.e. the optimised 1-D filter coefficients are used to filter in each coordinate direction.

In a similar fashion, we can also define a discrete reconstruction operation (de-filtering) as

$$R_\Delta[\bar{u}_i] = u_i^* = V_d^N \circledast \bar{u}_i = \sum_{l=-M_{IF}}^{M_{IF}} \beta_l \bar{u}_{i+l}, \tag{4.6}$$

where V_d^N is an approximate discrete inverse filter now acting on the filtered field. The superscript N denotes that this filter corresponds to the same operator obtained by applying N van Cittert iterations on the filtered field while M_{IF} is the stencil size of the inverse filter.

983 A47-12

It is straightforward to show that the transfer function of V_d^N is given by (Nikolaou *et al.* 2023)

$$\hat{V}_d(k_r) = \sum_{l=-M_{IF}}^{M_{IF}} \beta_l e^{jk_r h l} = g_0 + 2 \sum_{l=1}^{M_{IF}} \beta_l \cos(k_r h l), \tag{4.7}$$

and is completely determined by the coefficients β_l. In order to obtain these coefficients we solve the optimisation problem

$$\arg\min_{\beta_l} \left(\int_{kh=0}^{\pi} \left(\hat{V}_d^N(kh; \beta_l) \hat{G}_d(kh; g_l) - \hat{Q}_d^N(kh; g_l) \right)^2 d(kh) \right), \tag{4.8}$$

where $\hat{Q}_d^N(kh; g_l)$ is the discrete transfer function of the reconstructed signal obtained using N van Cittert iterations with a forward discrete filter G_d,

$$\hat{Q}_d^N(k_r) = 1 - \left(1 - b\hat{G}_d(k_r) \right)^N \left(1 - \hat{G}_d(k_r) \right). \tag{4.9}$$

Note that b is a constant typically taken to equal unity. We further impose the constraints,

$$\beta_0 + 2 \sum_{l=1}^{M_{IF}} \beta_l = 1, \tag{4.10}$$

$$\beta_0 + 2 \sum_{l=1}^{M_{IF}} \beta_l \cos(k_r h l) < (N+1) \quad \text{for all, } k_r h \in (0, \pi]. \tag{4.11}$$

The first constraint ensures that $\hat{V}_d^N(0) = 1$ and the second ensures that the upper bound is not exceeded (Nikolaou *et al.* 2023). It is important to note that the half-stencil size of the inverse filter M_{IF} need not be equal to the half-stencil size of the forward filter M. In practice, we take the following steps in order to compute optimised inverse filter coefficients β_l.

(i) For a given actual filter transfer function $\hat{G}$, solve the optimisation problem in (4.3) to obtain an optimised discrete forward filter with coefficients g_l and a transfer function $\hat{G}_d$.
(ii) Specify the number of van Cittert iterations N and calculate $\hat{Q}_d^N(k_r h; gl)$.
(iii) Specify the optimisation error and solve the optimisation problem in (4.8) to obtain β_l, each time adjusting the stencil size M_{IF} until the target optimisation error is obtained.

Reconstruction in the 3-D case is performed by applying the 1-D inverse filter operator in each coordinate direction. The reconstruction operator can be applied on $\bar{\rho}$ and $\overline{\rho\phi}$ to obtain higher-order reconstructions simply by increasing N and solving a new optimisation problem to obtain the corresponding coefficients, and the variance modelled following the procedure outlined in § 3. In other words, the modelling procedure remains the same, all that changes is the reconstruction operator R_Δ for which we now have an automated procedure through which its accuracy can be made arbitrarily high/low.

Forward filter		Inverse filter	
γ	4	N	5
$k_f h$	1.016	$k_f h$	1.825
M	4	M_{IF}	4
g_0	$3.4541548066530248 \times 10^{-1}$	β_0	$3.4854421863613538 \times 10^{0}$
g_1	$2.3756559200884170 \times 10^{-1}$	β_1	$-1.2481478317981463 \times 10^{0}$
g_2	$7.7013518685369819 \times 10^{-2}$	β_2	$-1.5529293982071232 \times 10^{-1}$
g_3	$1.1900936808129101 \times 10^{-2}$	β_3	$1.8924837810742531 \times 10^{-1}$
g_4	$8.1221216500810569 \times 10^{-4}$	β_4	$-2.8528699669243762 \times 10^{-2}$

Table 3. Optimised discrete explicit forward and inverse filter coefficients and properties for $\gamma = 4$. Note that the filters are symmetric, hence, $g_{-l} = g_l$ and $\beta_{-l} = \beta_l$.

4.1. *Optimised inverse filters*

The number of iterations N is an input parameter for the above optimisation problem. In practical LES, and using the classic iterative van Cittert algorithm, 3–5 iterations were used in previous works (Stolz & Adams 1999, 2001). In fact, $N = 5$ is sufficient to recover the filter's cutoff wavenumber k_f defined as $\hat{G}(k_f) = 0.5$. For larger N, wavenumbers that are damped by more than 50 % are recovered, which may not be desirable in practical LES. For instance, the performance of a second-order accurate centred numerical scheme (typical of most LES solvers) drops substantially after about $kh > 1$ (Lele 1992) and these wavenumbers should not be recovered. In practical LES, Δ/h that determines k_f should in principle be chosen such that wavenumbers beyond which the accuracy of the numerical scheme deteriorates are not recovered. In this work, $\Delta/h = 4$ is used that results in $k_f h \simeq 1$, and which ensures that the filtered fields are well resolved as per the criterion developed in earlier work (Nikolaou & Vervisch 2018). As a result, we also use $N = 5$ to solve the optimisation problem in an effort to mimic what would be done in actual LES. Note that in principle, we can increase N and obtain ever improved models; however, in practice, as N increases, so does the range of higher wavenumbers being recovered. As a result, an ever-increasing stencil size M_{IF} would be required that would make reconstruction more expensive – the exact M_{IF} threshold of when this process becomes more expensive than using iterative reconstruction has been derived in our earlier work (Nikolaou *et al.* 2023). The choice $N = 5$ results in an explicit inverse filter for the $\gamma = 4$ case with $M_{IF} = M = 5$, and the inverse filter reconstruction being about 5 times faster than iterative reconstruction according to the criterion derived (and validated) by Nikolaou *et al.* (2023).

Tables 3 and 4 list the important parameters for the optimised forward and inverse discrete Gaussian filters obtained by solving the above two optimisation problems for $\gamma = 4$ and $\gamma = 8$, respectively, while figure 1 shows the corresponding transfer functions of the actual/discrete forward/inverse filters. Note how the filter cutoff wavenumber increases when applying the inverse filter (almost doubles) that signifies the reconstruction of the damped wavenumbers. Clearly, both at the filtering and reconstruction levels the optimised discrete filters closely match the actual corresponding transfer functions. Application of the inverse filter to $\bar{\rho}$, $\overline{\rho\phi}$, and then following the procedure outlined in § 3 leads to a new base static model for the scalar variance known as the deconvolution-inverse filter (DEIF) model. For more details on the numerical implementation, the effect of using different filters (Helmholtz, implicit, etc.), different iteration counts N and so on, we refer the reader to our earlier work (Nikolaou *et al.* 2023).

Forward filter		Inverse filter	
γ	8	N	5
$k_f h$	0.508	$k_f h$	0.912
M	8	M_{IF}	8
g_0	$1.7281235518838708 \times 10^{-1}$	β_0	$3.6225796969507149 \times 10^{0}$
g_1	$1.5727024335484499 \times 10^{-1}$	β_1	$-2.0114664835843585 \times 10^{-1}$
g_2	$1.1875047232243820 \times 10^{-1}$	β_2	$-8.5901296273738481 \times 10^{-1}$
g_3	$7.4326164362626373 \times 10^{-2}$	β_3	$-5.2702491452982902 \times 10^{-1}$
g_4	$3.8552094759875553 \times 10^{-2}$	β_4	$1.5576346690679571 \times 10^{-1}$
g_5	$1.6581685041517420 \times 10^{-2}$	β_5	$1.9140276795709291 \times 10^{-1}$
g_6	$5.9354294696557794 \times 10^{-3}$	β_6	$-2.9855846257031377 \times 10^{-1}$
g_7	$1.7673745940579428 \times 10^{-3}$	β_7	$3.5288499249418004 \times 10^{-1}$
g_8	$4.1035850079021625 \times 10^{-4}$	β_8	$-1.2559808763746258 \times 10^{-1}$

Table 4. Optimised discrete explicit forward and inverse filter coefficients and properties for $\gamma = 8$. Note that the filters are symmetric, hence, $g_{-l} = g_l$ and $\beta_{-l} = \beta_l$.
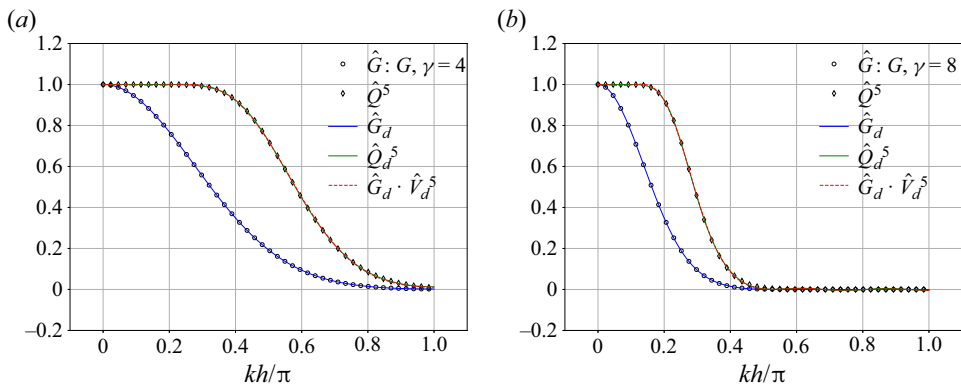

Figure 1. Actual transfer function of a Gaussian filter $\hat{G}$, actual reconstructed transfer function $\hat{Q}^N$ obtained using $N = 5$ van Cittert iterations, discrete transfer function of optimised filter $\hat{G}_d$, discrete reconstructed transfer function $\hat{Q}_d^N$ obtained using van Cittert iterations and the product between the discrete forward filter transfer function and the optimised inverse discrete filter transfer function $\hat{G}_d \hat{V}_d^N$: (a) $\gamma = 4$ and (b) $\gamma = 8$.

5. Dynamic models

5.1. *The classic dynamic gradient model revisited*

The purpose of this section is to discuss the well-known dynamic gradient model. This will serve as a prelude to § 5.2 where the dynamic procedure will be reinterpreted in the context of reconstruction modelling. In turn, this will enable us to derive a structured framework for developing general dynamic models for arbitrary reconstruction operators.

The dynamic procedure was originally introduced by Germano *et al.* (1991) for modelling the unresolved Reynolds stresses, specifically to correct the predictions of the static Smagorinsky model (Smagorinsky 1963) that was found to be too dissipative in the near-wall region. The procedure was later used to develop a dynamic variance model by Pierce & Moin (1998). In this procedure, the base static gradient model is corrected using

a dynamic parameter C_d,

$$\sigma^2 = C_d \Delta^2 \frac{\partial \tilde{\phi}}{\partial x_i} \frac{\partial \tilde{\phi}}{\partial x_i}, \tag{5.1}$$

which must be determined. The original dynamic evaluation of C_d essentially involved the following two assumptions.

   (i) The dynamic parameter C_d remains constant between the two filtering levels, at least locally and over the region spanned by the test filter $\hat{\Delta}$.

  (ii) The filter itself is idempotent, i.e. $\hat{\hat{\phi}} = \hat{\phi}$.

Here $\hat{}$ denotes filtering with a filter having a characteristic length scale $\hat{\Delta} > \Delta$ (typically $\hat{\Delta} = 2\Delta$). We now derive the original expression for C_d formally using the above two assumptions, and next we derive an alternative expression for the model's dynamic parameter irrespective of the filter properties. To proceed, we write (5.1) as

$$\overline{\rho\phi^2} - \bar{\rho}\tilde{\phi}\tilde{\phi} = C_d \Delta^2 \bar{\rho} \frac{\partial \tilde{\phi}}{\partial x_i} \frac{\partial \tilde{\phi}}{\partial x_i}, \tag{5.2}$$

which we test filter to obtain

$$\widehat{\overline{\rho\phi^2}} - \widehat{\bar{\rho}\tilde{\phi}\tilde{\phi}} = C_d \Delta^2 \left(\bar{\rho} \frac{\partial \tilde{\phi}}{\partial x_i} \frac{\partial \tilde{\phi}}{\partial x_i} \right)^{\widehat{}}. \tag{5.3}$$

Defining $\check{\phi} = \widehat{\bar{\rho}\tilde{\phi}}/\hat{\bar{\rho}}$ (for filtering operations, refer to table 2), the above can be neatly written as

$$\check{\tilde{\phi}^2} - \left(\tilde{\phi}\tilde{\phi} \right)^{\check{}} = C_d \Delta^2 \left(\frac{\partial \tilde{\phi}}{\partial x_i} \frac{\partial \tilde{\phi}}{\partial x_i} \right)^{\check{}}, \tag{5.4}$$

which involves the unresolved quantity $\check{\tilde{\phi}^2}$. The objective is to obtain a second expression involving $\check{\tilde{\phi}^2}$ and solve for C_d. Provided the filter is idempotent we may immediately write an expression for the variance at the test-filter level, i.e.

$$\frac{\widehat{\overline{\rho\phi^2}}}{\hat{\rho}} - \frac{\widehat{\overline{\rho\phi}}}{\hat{\rho}} \frac{\widehat{\overline{\rho\phi}}}{\hat{\rho}} = C_d \hat{\Delta}^2 \frac{\partial(\widehat{\overline{\rho\phi}}/\hat{\rho})}{\partial x_i} \frac{\partial(\widehat{\overline{\rho\phi}}/\hat{\rho})}{\partial x_i}, \tag{5.5}$$

which because of the filter idempotency assumption is equivalent to

$$\frac{\widehat{\overline{\rho\phi^2}}}{\hat{\bar{\rho}}} - \frac{\widehat{\overline{\rho\phi}}}{\hat{\bar{\rho}}} \frac{\widehat{\overline{\rho\phi}}}{\hat{\bar{\rho}}} = C_d \hat{\Delta}^2 \frac{\partial(\widehat{\overline{\rho\phi}}/\hat{\bar{\rho}})}{\partial x_i} \frac{\partial(\widehat{\overline{\rho\phi}}/\hat{\bar{\rho}})}{\partial x_i} \tag{5.6}$$

or

$$\check{\tilde{\phi}^2} - \check{\tilde{\phi}}\check{\tilde{\phi}} = C_d \hat{\Delta}^2 \frac{\partial \check{\tilde{\phi}}}{\partial x_i} \frac{\partial \check{\tilde{\phi}}}{\partial x_i}. \tag{5.7}$$

It is important to note that, for non-idempotent filters, the equivalent filter incorporating the effects of both the original and test filters should be used in order to write down an

983 A47-16

expression for the variance at the test-filter level – in the original works by Germano *et al.* (1991) this was denoted using $\hat{\bar{\Delta}}$, where $\bar{\Delta}$ stood for the original filter (denoted here as Δ).

Equations (5.4) and (5.7) can now be used to solve for C_d. In practice however, using (5.4) and (5.7) to calculate C_d may lead to instabilities (Pierce & Moin 1998). The alternative approach used by Pierce & Moin (1998) is to calculate C_d using

$$C_d^M = \frac{\langle LM^P \rangle}{\langle M^P M^P \rangle} \tag{5.8}$$

instead. In the expression above, $L = \widehat{\bar{\rho}\tilde{\phi}\tilde{\phi}} - \hat{\bar{\rho}}\check{\tilde{\phi}}\check{\tilde{\phi}}$ is the Leonard term and $M^P = \hat{\Delta}^2\hat{\bar{\rho}}|\nabla\check{\tilde{\phi}}|^2 - \Delta^2\widehat{\bar{\rho}|\nabla\tilde{\phi}|^2}$ is the model term. This approach is analogous to the least-squares minimisation approach proposed by Lilly (1992) for calculating the dynamic parameter in the Smagorinsky model for the Reynolds stresses (excluding the averaging in the nominator and denominator). The brackets $\langle \rangle$ typically denote averaging in statistically homogeneous directions, and serve to further stabilise C_d (Pierce & Moin 1998). If no homogeneous directions exist, an alternative integral-based formulation can be used instead proposed by Ghosal *et al.* (1995).

For non-idempotent filters, we can use the results of §3 to derive an approximate expression of the unresolved quantity $\check{\tilde{\phi^2}}$ without invoking the idempotency assumption. A similar procedure was employed by Balarac *et al.* (2008) in order to derive an improved expression for the dynamic parameter of a gradient-based model for the scalar variance in the case of constant-density flows. Extending the procedure to variable-density flows we have, from (3.19),

$$\bar{\rho}\widetilde{\phi^2} = \bar{\rho}\tilde{\phi}\tilde{\phi} + 2a_2\bar{\rho}\frac{\partial\tilde{\phi}}{\partial x_i}\frac{\partial\tilde{\phi}}{\partial x_i}, \tag{5.9}$$

which we test filter to obtain

$$\widehat{\bar{\rho}\widetilde{\phi^2}} = \widehat{\bar{\rho}\tilde{\phi}\tilde{\phi}} + 2a_2\left(\bar{\rho}\frac{\partial\tilde{\phi}}{\partial x_i}\frac{\partial\tilde{\phi}}{\partial x_i}\right)^{\hat{}} \tag{5.10}$$

or

$$\check{\tilde{\phi^2}} = \left(\tilde{\phi}\tilde{\phi}\right)^{\check{}} + 2a_2\left(\frac{\partial\tilde{\phi}}{\partial x_i}\frac{\partial\tilde{\phi}}{\partial x_i}\right)^{\check{}} = \check{\tilde{\phi}}\check{\tilde{\phi}} + 2a_2'\frac{\partial\check{\tilde{\phi}}}{\partial x_i}\frac{\partial\check{\tilde{\phi}}}{\partial x_i} + 2a_2\left(\frac{\partial\tilde{\phi}}{\partial x_i}\frac{\partial\tilde{\phi}}{\partial x_i}\right)^{\check{}}, \tag{5.11}$$

where the second step follows by expanding $(\tilde{\phi}\tilde{\phi})^{\check{}}$ using (3.19) at the test-filter level (a_2' corresponding to the test-filter second moment using $\hat{\Delta}$ instead of Δ). In order to correct the above base static model by taking into account SGS effects through a dynamic parameter C_d, the dynamic model should be proportional to both $a_2(\partial\tilde{\phi}/\partial x_i\partial\tilde{\phi}/\partial x_i)^{\check{}}$ and $(a_2'\partial\check{\tilde{\phi}}/\partial x_i\partial\check{\tilde{\phi}}/\partial x_i)$. Since a_2 is proportional to Δ^2, and a_2' is proportional to $\hat{\Delta}^2$ the dynamic formulation should read

$$\check{\tilde{\phi^2}} - \check{\tilde{\phi}}\check{\tilde{\phi}} = C_d\hat{\Delta}^2\frac{\partial\check{\tilde{\phi}}}{\partial x_i}\frac{\partial\check{\tilde{\phi}}}{\partial x_i} + C_d\Delta^2\left(\frac{\partial\tilde{\phi}}{\partial x_i}\frac{\partial\tilde{\phi}}{\partial x_i}\right)^{\check{}}. \tag{5.12}$$

In contrast to (5.7), (5.12) contains an additional term that is the filtered gradient product. Solving for C_d using (5.4) and (5.12) and regularising, we obtain an alternative expression

for the dynamic parameter,

$$C_d^B = \frac{\langle LM^B \rangle}{\langle M^B M^B \rangle}. \tag{5.13}$$

In the above expression, the Leonard term remains the same, but the model term is now $M^B = \hat{\Delta}^2 \hat{\bar{\rho}} |\nabla \check{\tilde{\phi}}|^2$. For constant-density flows, (5.13) reduces to that of Balarac *et al.* (2008), which was shown to provide improved predictions for the scalar variance in the case of a non-reactive scalar under forced homogeneous isotropic turbulence. The assumptions involved in deriving (5.8) were shown by Balarac *et al.* (2008) not to be verified, at least when using non-idempotent filters as was done in the original derivation of the method (Pierce & Moin 1998). This leads to the p.d.f. of C_d having substantial probabilities/contributions over a wide range of negative values that of course leads to negative, i.e. unrealisable variance predictions (Balarac *et al.* 2008). In contrast, C_d^B is always positive by construction. Furthermore, the evaluation of the dynamic parameter using (5.13) was shown to be more robust (Balarac *et al.* 2008). For reacting scalars, a thorough *a priori* testing of both the C_d^M and C_d^B formulations was conducted by Knudsen *et al.* (2010) using DNS data of statistically planar turbulent premixed flames. The testing was conducted for a wide range of Δ values. For small Δ, (5.13) improved the predictions substantially in line with the results of Balarac *et al.* (2008). For larger Δ, it was found that both formulations, but also even the static gradient model, all resulted in similar performances. On this point, it is interesting to note that Mukhopadhyay *et al.* (2015) conducted both *a priori* and *a posteriori* studies of turbulent premixed Bunsen flames using both the static and the dynamic gradient model (using C_d^M), and it was concluded that the dynamic model did not improve the predictions over its static counterpart. Therefore, the overall evidence appears to suggest that the improvements obtained by a dynamic procedure might be limited by the filter size.

5.2. *A reconstruction-based interpretation of the dynamic procedure*

The role of a dynamic procedure is to correct a base static model, call this B_m. However, in LES the unresolved variance is unknown, and the only information available to correct B_m are the LES variables $\bar{\rho}$, $\overline{\rho\phi}$, etc. Nevertheless, from the resolved variables one can calculate a corresponding resolved variance σ_r^2 – an equivalent resolved stress tensor was used for developing a dynamic model for the unresolved Reynolds stresses by Liu, Meneveau & Katz (1994). If the resolved variance is modelled using a model T_m, a natural approach is to try to correct the base model of the unresolved variance using σ_r^2 and T_m. In fact, the Leonard term in the expression for C_d^B in (5.13) (numerator) divided by $\hat{\bar{\rho}}$ is the resolved variance σ_r^2 at the test-filter level,

$$\sigma_r^2 = \frac{\widehat{\bar{\rho}\tilde{\phi}\tilde{\phi}}}{\hat{\bar{\rho}}} - \left(\frac{\widehat{\bar{\rho}\tilde{\phi}}}{\hat{\bar{\rho}}} \right)^2 = \left(\tilde{\phi}\tilde{\phi} \right)^{\check{}} - \check{\tilde{\phi}}\check{\tilde{\phi}} = \frac{L}{\hat{\bar{\rho}}}. \tag{5.14}$$

Also, the remaining denominator term in (5.13) $\hat{\Delta}^2 |\nabla \check{\tilde{\phi}}|^2$ is in fact a gradient model T_m for the resolved variance. Therefore, the expression for C_d^B in (5.13) can also be written as σ_r^2 / T_m, which is the ratio between the resolved and the modelled resolved variance at the test-filter level. This ratio can be interpreted as a measure of the error in modelling the resolved variance σ_r^2 using T_m. We may therefore express the

scale-similarity assumption as

$$\frac{\sigma^2}{B_m} \simeq \frac{\sigma_r^2}{T_m} \simeq C_d^N, \tag{5.15}$$

essentially stating that the error in approximating the unresolved variance σ^2 using a base model B_m scales as the error in modelling the resolved variance σ_r^2 using a base model T_m. Regularisation ($\langle \rangle$) of the dynamic parameter C_d^N then leads to the following expression of the dynamic model:

$$\sigma^2 = B_m \frac{\langle \sigma_R^2 T_m \rangle}{\langle T_m T_m \rangle} = B_m C_d^N. \tag{5.16}$$

As shown in § 3, the gradient model is a subset model of more general reconstruction base models B_m such as SM4 and AD4. Therefore, if B_m is a general reconstruction-based model, a natural approach to obtain a model T_m for the resolved variance is to use reconstruction as well but at the test-filter level. Denoting $\rho_L = \bar{\rho}$ and $\phi_L = \tilde{\phi}$ we can write the resolved variance as

$$\sigma_r^2 = \frac{\widehat{\rho_L \phi_L \phi_L}}{\hat{\rho}_L} - \left(\frac{\widehat{\rho_L \phi_L}}{\hat{\rho}_L} \right)^2 = (\phi_L \phi_L)^{\check{}} - \check{\phi}_L \check{\phi}_L. \tag{5.17}$$

Clearly, the above equation is analogous to the definition of the unresolved variance, the only difference being the filter size and the definition of the Favre averaging. We are now in a position to write the reconstruction model at the test-filter level for σ_r^2 as

$$T_m = \frac{\widehat{\rho_L^* \phi_L^* \phi_L^*}}{\hat{\rho}_L^*} - \left(\frac{\widehat{\rho_L^* \phi_L^*}}{\hat{\rho}_L^*} \right)^2 = \left(\phi_L^* \phi_L^* \right)^{\check{}} - \left(\check{\phi}_L^* \right)^2, \tag{5.18}$$

where ρ_L^* and $\phi_L^* = (\rho\phi)_L^*/\rho_L^*$ are the reconstruction estimates at the test-filter level. Specifically, denoting the reconstruction operator at the test-filter level as $R_{\hat{\Delta}}$, the reconstructions at the test-filter level are given by $\rho_L^* = R_{\hat{\Delta}}[\hat{\bar{\rho}}]$ and $(\rho\phi)_L^* = R_{\hat{\Delta}}[\widehat{\overline{\rho u}}]$. Provided $\phi_L^* \in [0, 1]$ then $\check{\phi}_L^* \in [0, 1]$ as well, and $T_m \in [0, \check{\phi}_L^*(1 - \check{\phi}_L^*)]$ ensuring that the modelled resolved variance is bounded. Also, since $\sigma_r^2 \in [0, \check{\phi}_L(1 - \check{\phi}_L)]$, $C_d^N \geq 0$ and the variance predictions are always positive. Furthermore, in the limit $R_{\Delta}[\bar{\phi}] \to \phi$ and $R_{\hat{\Delta}}[\hat{\bar{\phi}}] \to \bar{\phi}$, $B_m \to \sigma^2$ while $T_m \to \sigma_r^2$, therefore, $C_d^N \to 1$, and the dynamic model recovers the actual variance.

The reconstruction operator $R_{\hat{\Delta}}$ acting on the test-filtered variables can be obtained using the same procedure as in § 3 but at the test-filter level. For example, using truncated Taylor-series expansions we have, for a general variable $\hat{u}_L = \hat{\bar{u}}$, the reconstruction estimate

$$R_{\hat{\Delta}}[\hat{\bar{u}}] = u_L^* = \hat{u}_L - a_2' \nabla^2 \hat{u}_L + O(\hat{\Delta}^4) = \hat{\bar{u}} - a_2' \nabla^2 \hat{\bar{u}} + O(\hat{\Delta}^4), \tag{5.19}$$

where a_2' is the filter's second moment but using $\hat{\Delta}$ instead of Δ (see table 1). As an example, for an $O(\hat{\Delta}^2)$ reconstruction at the test-filter level: $\rho_L^* = \hat{\rho}_L = \hat{\bar{\rho}}$, $(\rho\phi)_L^* = \widehat{\rho_L \phi_L} = \widehat{\bar{\rho}\tilde{\phi}}$ and $\phi_L^* = \widehat{\bar{\rho}\tilde{\phi}}/\hat{\bar{\rho}} = \check{\phi}$. Inserting these reconstructions in (5.18) we obtain an

983 A47-19

equivalent SM2 model for the resolved variance,

$$T_m = \frac{\widehat{\hat{\rho}\check{\tilde{\phi}}\check{\tilde{\phi}}}}{\hat{\hat{\rho}}} - \left(\frac{\widehat{\hat{\rho}\check{\tilde{\phi}}}}{\hat{\hat{\rho}}}\right)^2 = \left(\check{\tilde{\phi}}\check{\tilde{\phi}}\right)^{\smallfrown} - \overset{\circ}{\check{\phi}}\overset{\circ}{\check{\phi}}, \qquad (5.20)$$

and the dynamic parameter for the SM2 model (with regularisation) becomes

$$C_d^N = \frac{\left\langle \left(\left(\tilde{\phi}\tilde{\phi}\right)^{\smallsmile} - \overset{\circ}{\check{\phi}}\overset{\circ}{\check{\phi}}\right)\left(\left(\check{\tilde{\phi}}\check{\tilde{\phi}}\right)^{\smallfrown} - \overset{\circ}{\check{\phi}}\overset{\circ}{\check{\phi}}\right)\right\rangle}{\left\langle \left(\left(\check{\tilde{\phi}}\check{\tilde{\phi}}\right)^{\smallfrown} - \overset{\circ}{\check{\phi}}\overset{\circ}{\check{\phi}}\right)\left(\left(\check{\tilde{\phi}}\check{\tilde{\phi}}\right)^{\smallfrown} - \overset{\circ}{\check{\phi}}\overset{\circ}{\check{\phi}}\right)\right\rangle}. \qquad (5.21)$$

The overall dynamic SM2 model, call this DSM2-N, is just the base static SM2 model of (3.11) corrected using the above expression for the dynamic parameter,

$$\sigma^2 = C_d^N \left(\left(\tilde{\phi}\tilde{\phi}\right)^{\smallsmile} - \overset{\circ}{\check{\phi}}\overset{\circ}{\check{\phi}}\right). \qquad (5.22)$$

For an $O(\hat{\Delta}^4)$ reconstruction on the other hand: $\rho_L^* = \hat{\rho}_L - a_2'\nabla^2\hat{\rho}_L + O(\hat{\Delta}^4) = \hat{\hat{\rho}} - a_2'\nabla^2\hat{\hat{\rho}} + O(\hat{\Delta}^4)$ and $(\rho\phi)_L^* = \widehat{(\rho\phi)_L} - a_2'\nabla^2\widehat{(\rho\phi)_L} + O(\hat{\Delta}^4) = \widehat{\hat{\rho\phi}} - a_2'\nabla^2(\widehat{\hat{\rho\phi}}) + O(\hat{\Delta}^4)$. As before, $\phi_L^* = (\rho\phi)_L^*/\rho_L^*$. Inserting these reconstructions in (5.18) and following the same procedure as in §3, we eventually obtain an equivalent SM4 model for the resolved variance,

$$T_m = \left(\check{\tilde{\phi}}\check{\tilde{\phi}}\right)^{\smallfrown} - \overset{\circ}{\check{\phi}}\overset{\circ}{\check{\phi}} + \frac{2a_2'}{\hat{\hat{\rho}}}\left(\overset{\circ}{\check{\phi}}\nabla^2\widehat{\hat{\rho}\check{\tilde{\phi}}} - \widehat{\check{\phi}\nabla^2\hat{\rho}\check{\phi}}\right) + \frac{a_2'}{\hat{\hat{\rho}}}\left(\widehat{\check{\tilde{\phi}}\check{\tilde{\phi}}\nabla^2\hat{\rho}} + \left(\check{\tilde{\phi}}\check{\tilde{\phi}}\right)^{\smallfrown}\nabla^2\hat{\hat{\rho}} - 2\overset{\circ}{\check{\phi}}\overset{\circ}{\check{\phi}}\nabla^2\hat{\hat{\rho}}\right). \qquad (5.23)$$

Expanding the test-filtering operations up to $O(\hat{\Delta}^4)$ in the above SM4 model, as done in §3, it is straightforward to show after some algebraic manipulation that the above expression reduces to

$$T_m = 2a_2'\frac{\partial\check{\tilde{\phi}}}{\partial x_i}\frac{\partial\check{\tilde{\phi}}}{\partial x_i}, \qquad (5.24)$$

which is the equivalent gradient model for the resolved variance at the test-filter level. For a Gaussian filter, $a_2' = \hat{\Delta}^2/24$ in which case we recover the gradient model for the resolved variance employed in the classic dynamic models. Therefore, the expression for the model term in (5.13) is a subset of the more general model in (5.23). As a result, if the expression in (5.23) is used to develop a dynamic model, we obtain (with regularisation)

$$C_d^N = \frac{\left\langle\left(\left(\tilde{\phi}\tilde{\phi}\right)^{\smallsmile} - \overset{\circ}{\check{\phi}}\overset{\circ}{\check{\phi}}\right)\left(\left(\check{\tilde{\phi}}\check{\tilde{\phi}}\right)^{\smallfrown} - \overset{\circ}{\check{\phi}}\overset{\circ}{\check{\phi}} + \frac{2a_2'}{\hat{\hat{\rho}}}\left(\overset{\circ}{\check{\phi}}\nabla^2\widehat{\hat{\rho}\check{\tilde{\phi}}} - \widehat{\check{\phi}\nabla^2\hat{\rho}\check{\phi}}\right) + \frac{a_2'}{\hat{\hat{\rho}}}\left(\widehat{\check{\tilde{\phi}}\check{\tilde{\phi}}\nabla^2\hat{\rho}} + \left(\check{\tilde{\phi}}\check{\tilde{\phi}}\right)^{\smallfrown}\nabla^2\hat{\hat{\rho}} - 2\overset{\circ}{\check{\phi}}\overset{\circ}{\check{\phi}}\nabla^2\hat{\hat{\rho}}\right)\right)\right\rangle}{\left\langle\left(\left(\check{\tilde{\phi}}\check{\tilde{\phi}}\right)^{\smallfrown} - \overset{\circ}{\check{\phi}}\overset{\circ}{\check{\phi}} + \frac{2a_2'}{\hat{\hat{\rho}}}\left(\overset{\circ}{\check{\phi}}\nabla^2\widehat{\hat{\rho}\check{\tilde{\phi}}} - \widehat{\check{\phi}\nabla^2\hat{\rho}\check{\phi}}\right) + \frac{a_2'}{\hat{\hat{\rho}}}\left(\widehat{\check{\tilde{\phi}}\check{\tilde{\phi}}\nabla^2\hat{\rho}} + \left(\check{\tilde{\phi}}\check{\tilde{\phi}}\right)^{\smallfrown}\nabla^2\hat{\hat{\rho}} - 2\overset{\circ}{\check{\phi}}\overset{\circ}{\check{\phi}}\nabla^2\hat{\hat{\rho}}\right)\right)^2\right\rangle}. \qquad (5.25)$$

It is important to note that in contrast to the dynamic parameter for the SM2 model, the above expression is not necessarily always positive as a result of truncating the filtering

983 A47-20

operations to obtain the expression for T_m. The dynamic SM4 model DSM4-N then becomes

$$\sigma^2 = C_d^N \left(\left(\widetilde{\tilde{\phi}\tilde{\phi}} \right)^{\smallsmile} - \check{\tilde{\phi}}\check{\tilde{\phi}} + \frac{2a_2}{\bar{\bar{\rho}}} \left(\check{\tilde{\phi}}\nabla^2 \overline{\bar{\rho}\tilde{\phi}} - \overline{\tilde{\phi}\nabla^2 \bar{\rho}\tilde{\phi}} \right) \right.$$

$$\left. + \frac{a_2}{\bar{\bar{\rho}}} \left(\overline{\tilde{\phi}\tilde{\phi}\nabla^2 \bar{\rho}} + \left(\widetilde{\tilde{\phi}\tilde{\phi}} \right)^{\smallsmile} \nabla^2 \bar{\rho} - 2\check{\tilde{\phi}}\check{\tilde{\phi}}\nabla^2 \bar{\bar{\rho}} \right) \right). \tag{5.26}$$

As shown above, the dynamic procedure employed in classic algebraic dynamic models is essentially a two-level approximate reconstruction-based modelling approach. At the normal filter level Δ reconstruction serves to obtain a base model B_m for the unresolved variance σ^2 while at the test-filter level $\hat{\Delta}$ it serves to obtain a model T_m for the resolved variance σ_r^2. Then, by employing the scale-similarity assumption through (5.16) the ratio of the resolved variance to the modelled resolved variance is used to correct the variance prediction of the base static model.

5.3. *Generalized dynamic reconstruction models*

In this section we consolidate all the results thus far in an effort to present a general methodology for obtaining a dynamic model for any given general reconstruction operator R_Δ acting on the LES fields, and for any reconstruction operator $R_{\hat{\Delta}}$ acting on the test-filtered LES fields. This also includes bounding of the reconstructed fields. The overall model reads

$$\sigma^2 = C_d^N \left(\frac{\overline{\rho^* \phi^* \phi^*}}{\overline{\rho^*}} - \left(\frac{\overline{\rho^* \phi^*}}{\overline{\rho^*}} \right)^2 \right). \tag{5.27}$$

The bounded reconstructions at Δ are obtained using

$$\left. \begin{aligned} \rho^* &= \max(\min(R_\Delta[\bar{\rho}], \rho_h), \rho_l), \\ (\rho\phi)^* &= \max(\min(R_\Delta[\overline{\rho\phi}], (\rho\phi)_h), (\rho\phi)_l), \\ \phi^* &= \max(\min((\rho\phi)^*/\rho^*, 1), 0), \end{aligned} \right\} \tag{5.28}$$

and at $\hat{\Delta}$ by

$$\left. \begin{aligned} \rho_L^* &= \max(\min(R_{\hat{\Delta}}[\hat{\bar{\rho}}], \rho_h), \rho_l), \\ (\rho\phi)_L^* &= \max(\min(R_{\hat{\Delta}}[\widehat{\overline{\rho\phi}}], (\rho\phi)_h), (\rho\phi)_l), \\ \phi_L^* &= \max(\min((\rho\phi)_L^*/\rho_L^*, 1), 0). \end{aligned} \right\} \tag{5.29}$$

The dynamic parameter C_d^N is then calculated using

$$C_d^N = \frac{\left\langle \left(\left(\widetilde{\tilde{\phi}\tilde{\phi}} \right)^{\smallsmile} - \check{\tilde{\phi}}\check{\tilde{\phi}} \right) \left((\phi_L^* \phi_L^*)^{\smallsmile} - \check{\phi}_L^* \check{\phi}_L^* \right) \right\rangle}{\left\langle \left((\phi_L^* \phi_L^*)^{\smallsmile} - \check{\phi}_L^* \check{\phi}_L^* \right) \left((\phi_L^* \phi_L^*)^{\smallsmile} - \check{\phi}_L^* \check{\phi}_L^* \right) \right\rangle}. \tag{5.30}$$

Clearly, the above expression is always positive ensuring that we recover realisable predictions of the variance. As we will see in the sections that follow, in the case where $R_\Delta = (I - a_2\nabla^2)$ and $R_{\hat{\Delta}} = (I - a_2'\nabla^2)$ the above procedure results in a dynamic model

Model	Short name	Reference equation(s)
Static:		
$(\tilde{\phi}\tilde{\phi})^{\vee} - \breve{\tilde{\phi}}\breve{\tilde{\phi}}$	SM2	(3.11)
$(\tilde{\phi}\tilde{\phi})^{\vee} - \breve{\tilde{\phi}}\breve{\tilde{\phi}} + \dfrac{2a_2}{\bar{\bar{\rho}}}(\breve{\tilde{\phi}}\nabla^2\overline{\bar{\rho}\tilde{\phi}} - \overline{\tilde{\phi}\nabla^2\bar{\rho}\tilde{\phi}})+$	SM4	(3.15)
$\dfrac{a_2}{\bar{\bar{\rho}}}(\overline{\overline{\tilde{\phi}\tilde{\phi}}\nabla^2\bar{\rho}} + (\tilde{\phi}\tilde{\phi})^{\vee}\nabla^2\bar{\bar{\rho}} - 2\breve{\tilde{\phi}}\breve{\tilde{\phi}}\nabla^2\bar{\bar{\rho}})$		
$2a_2\dfrac{\partial\tilde{\phi}}{\partial x_i}\dfrac{\partial\tilde{\phi}}{\partial x_i}$	GR	(3.19)
$\widehat{\phi^*\phi^*} - \widehat{\phi^*}\widetilde{\phi^*}$	AD4	(3.12), (3.22), (3.23) and (3.24)
$\widetilde{\phi^*\phi^*} - \widetilde{\phi^*}\widetilde{\phi^*}$	DEIF	(3.22), (3.23) and (3.24)
Dynamic:		
$C_d^N \cdot$ SM2	DSM2-N	(5.21) and (5.22)
$C_d^N \cdot$ SM4	DSM4-N	(5.25) and (5.26)
$C_d^B\Delta^2\dfrac{\partial\tilde{\phi}}{\partial x_i}\dfrac{\partial\tilde{\phi}}{\partial x_i}$	DGR-B	(5.1) and (5.13)
$C_d^N \cdot$ AD4	DAD4-N	(3.12), (5.27) and (5.30)
$C_d^N \cdot$ DEIF	DEIF-N	(5.27) and (5.30)

Table 5. Summary of the various models tested and the relevant equations used. A Gaussian filter is used for all models for which $a_2 = \Delta^2/24$. Note that the parameter C_d^N is different for each model and calculated using the procedure outlined in § 5.2.

far superior than the DSM4-N model developed in the previous section. We will refer to this model as DAD4-N. Furthermore, in the case where the reconstruction operator is given by the optimised inverse discrete filter we will refer to this model as DEIF-N. Note that in this case optimised inverse filters are used both at the normal filter level Δ, and at the test filter $\hat{\Delta}$. At the normal filter level the inverse filter coefficients are listed in table 3 ($\gamma = 4$), and at the test-filter level the inverse filter coefficients are listed in table 4 ($\gamma = 8$).

6. Results

A summary of all the different models tested is given in table 5. These include five static models (SM2, SM4, GR, AD4, DEIF) and their dynamic versions (DSM2-N, DSM4-N, DGR-B, DAD4-N, DEIF-N). Here 'B' in the dynamic models indicates that the dynamic parameter is calculated using C_d^B from (5.13) (the dynamic gradient model with C_d^M is not considered due to its poorer performance in comparison), while N indicates using C_d^N. Note that the C_d^N formulation depends on the base static model used and the reconstruction operator used as outlined in § 5.2. The performance of each model is quantified by calculating the mean-squared error between the modelled variance σ_m^2 and the actual reference variance σ^2 as obtained on the LES mesh. This is defined using

$$e = \frac{1}{N_s}\sum_{\boldsymbol{x},t}\left(\sigma_m^2(\boldsymbol{x},t) - \sigma^2(\boldsymbol{x},t)\right)^2|_{\tilde{c}\in[\epsilon,1-\epsilon]}, \quad (6.1)$$

where $N_s = N_x N_y N_z N_t$ is the total sample size and $\epsilon = 0.05$. The conditioning on $\tilde{c} \in [\epsilon, 1-\epsilon]$ ensures that no-reaction regions are not sampled thereby biasing the results. This is because in no-reaction regions the scalar fields are more or less constant and filtering/reconstruction would be nearly perfect. The performance of each model is also
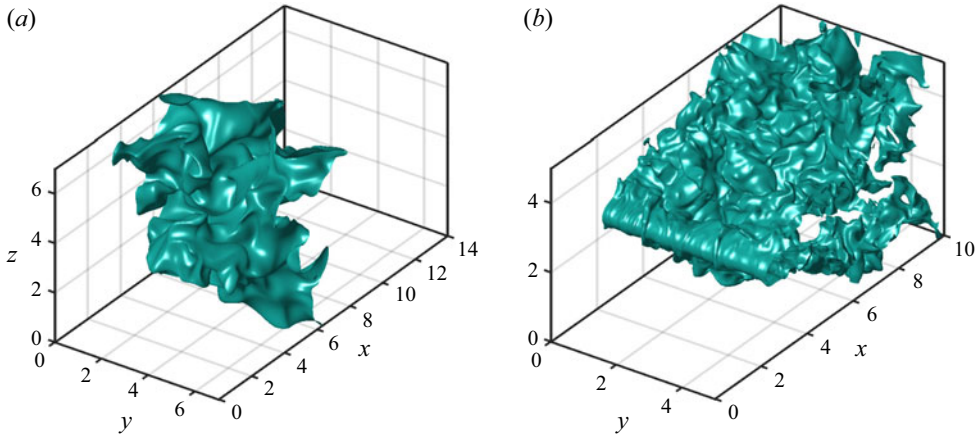
Figure 2. Progress-variable isosurface of the leading edge of the flame ($c = 0.1$) for (*a*) the planar flame and (*b*) the V-flame. Dimensions are in mm.

evaluated by calculating the conditional variance based on $\tilde{c}$ denoted by $\sigma^2|\tilde{c}$. The conditional averages are also time averaged $\langle \ \rangle$ over several samples in time to increase the statistical accuracy of the results. In the following section a brief description of the DNS databases used for testing is presented.

6.1. *The DNS databases*

The DNS databases correspond to two turbulent premixed flames simulated using detailed chemistry. Database PB corresponds to a statistically planar multi-component-fuel/air flame propagating in an inflow–outflow configuration, and database V97 is a statistically stationary hydrogen/air V-flame anchored on a fixed rod. In both cases, turbulent reactants enter from one end of the computational domain forming a flame that interacts with the incoming turbulence. Figure 2 shows the flow configuration for each flame. Flame PB was simulated using the in-house fully compressible solver SENGA2 (Cant 2012) and flame V97 using the TTX solver (Minamoto *et al.* 2011). The solver SENGA2 employs a tenth-order centred finite-difference scheme for the spatial derivatives and a fourth-order Runge–Kutta scheme for the time stepping, while TTX employs a fourth-order finite-difference scheme and a third-order Runge–Kutta scheme. Boundary conditions in both codes are implemented using the Navier–Stokes characteristics boundary conditions formalism (Thompson 1987; Poinsot & Lele 1992; Sutherland & Kennedy 2003).

Chemistry is modelled using a 49 reaction 15 species chemical mechanism for the planar flame (Nikolaou & Swaminathan 2013), and a 27 reaction 12 species chemical mechanism for the hydrogen/air flame (Gutheil, Balakrishnan & Williams 1993). Table 6 lists the important parameters for each database: u_{rms} is the root-mean-square value of the fluctuating component of the incoming turbulent velocity field, l_T is the turbulence integral length scale in the reactant side, the turbulence Reynolds number is $Re_T = u_{rms}l_T/\nu_r$, the Damkohler number is $Da = (l_T/u_{rms})/(\delta/s_L)$ and the Karlovitz number is $Ka = (\delta/\eta_k)^2$, where s_L is the laminar flame speed. The (diffusive) thickness is $\delta = \nu_r/s_L$. The laminar flame thickness is defined as $\delta_L = 1/\max(\mathrm{d}c/\mathrm{d}x)$, where c is the progress variable. The progress variable is defined using species mass fractions, i.e. $c = (Y - Y_r)/(Y_p - Y_r)$.

Database	s_L (m s^{-1})	δ_L (mm)	u_{rms}/s_L	l_T/δ	Re_T	Da	Ka	L_x (mm)	L_y (mm)	L_z (mm)
PB	2.5	0.64	9	16.7	150.1	1.9	6.6	14	7	7
V97	11.4	0.20	6	93.8	562.8	15.6	1.5	10	5	5

Table 6. Important flame parameters for the planar (PB) and V (V97) flames.

Case	Δ^+	N_x	N_y	N_z
PB	DNS	768	384	384
	1	89	45	45
	2	45	23	23
	3	31	15	15
V97	DNS	769	385	385
	1	201	101	101
	2	101	51	51
	3	67	34	34

Table 7. The DNS and LES meshes for $\Delta/h = 4$.

For the planar flame, c is based on the CO mass fraction, and for the V-flame it is based on the H_2 mass fraction. Further details of the simulations, numerical schemes, etc. can be found in Nikolaou & Swaminathan (2015) and Minamoto *et al.* (2011). As noted in table 6, the databases differ substantially in their thermo-chemical properties (laminar flame speed, flame thickness, etc.) and flow configuration (freely propagating and with mean shear). Note that even though the *Da* number for the planar flame is lower, the V-flame experiences smaller-scale wrinkling due to the presence of the rod that 're-energizes' the flow. In the planar flame, turbulence decays with downstream distance x and, as a result, the flame experiences larger-scale wrinkling as evidenced in figure 2(*a*). This has some important modelling consequences since reconstruction for the V-flame must recover a wider range of wavenumbers for an accurate variance estimation. Therefore, for the same reconstruction order, we would expect the variance predictions for the V-flame to be of lower accuracy.

The DNS data are filtered using a Gaussian filter: $G(x) = (6/(\pi\Delta)^2)^{3/2} \exp(-6x\cdot x/ \Delta^2)$. The analytic form of the filter is approximated in physical space using a 3-D discrete filtering operator that is constructed by the successive application of 1-D discrete filters in each coordinate direction. This implies that the discrete filter operator does not preserve the isotropy of the analytic filter. However, in practice, the filter width is sufficiently larger than the mesh spacing that ensures that any anisotropic effects are negligible. On the boundaries, the discrete filter is applied as usual taking into account the corresponding boundary conditions for each case. In order to simulate an LES, the filtered DNS data are then sampled from the DNS mesh onto a coarser LES mesh. The choice of the LES mesh size h is based on the criterion derived by Nikolaou & Vervisch (2018), specifically $h = \Delta/4$ is used. This criterion ensures that the filtered flame thickness is adequately resolved on the LES mesh. Table 7 shows for each filter size the corresponding LES mesh. Note that $\Delta^+ = \Delta/\delta_L$, and the range of Δ^+ values considered corresponds to well-resolved LES conditions – all three LES meshes are substantially coarser than the DNS mesh.

	Δ^+	SM2	SM4	GR	AD4	DEIF
PB						
	1	6.381×10^{-5}	1.470×10^{-5}	2.076×10^{-5}	8.738×10^{-6}	1.093×10^{-6}
	2	4.082×10^{-4}	1.725×10^{-4}	2.062×10^{-4}	1.137×10^{-4}	2.097×10^{-5}
	3	7.585×10^{-4}	3.837×10^{-4}	4.671×10^{-4}	2.748×10^{-4}	5.216×10^{-5}
V97						
	1	8.290×10^{-5}	1.963×10^{-5}	2.539×10^{-5}	1.300×10^{-5}	2.600×10^{-6}
	2	6.002×10^{-4}	2.183×10^{-4}	2.669×10^{-4}	1.436×10^{-4}	2.360×10^{-5}
	3	1.390×10^{-3}	6.281×10^{-4}	7.459×10^{-4}	4.320×10^{-4}	7.754×10^{-5}

Table 8. Mean-squared errors obtained using (6.1) for each of the static models.
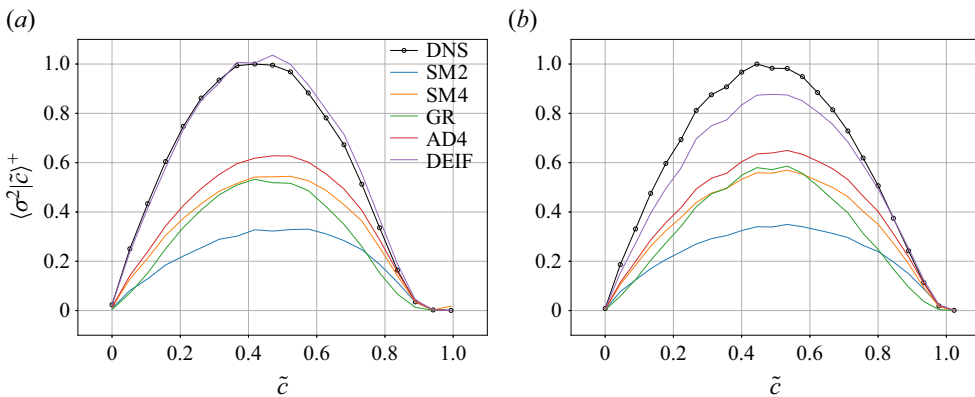
Figure 3. Conditionally averaged variance predictions of the static models against the reference variance at $\Delta^+ = 3$ for (*a*) the planar flame and (*b*) the V-flame. Note that these are normalised using the maximum of the reference conditional variance. Results are shown for (*a*) PB $-\Delta^+ = 3$, (*b*) V97 $-\Delta^+ = 3$.

6.2. *Static models*

In order to test the validity of the modelling framework developed in § 3 we begin by examining the performance of the base (static) models. Table 8 lists the errors for each model, and figure 3 shows the corresponding conditional averages. Instantaneous predictions for each model are shown for the V-flame in figure 4 (similar scatter plots were obtained for case PB). The results in table 8 indicate that the SM4 model substantially improves the predictions over the SM2 model for all three filter widths and for both databases. The SM4 model also performs better than the GR model that, as shown in § 3, is a subset of SM4. This behaviour is also evident in the instantaneous predictions shown in figure 4: the GR model has an inferior correlation with the reference variance, and a similar instantaneous distribution for this model was also obtained by Knudsen *et al.* (2010). Even though the SM4 model has some negative predictions these are very few, which contributes to the lower overall error for this model. The AD4 model, which is of the same reconstruction order ($O(\Delta^4)$) as the SM4 model, has substantially improved performance over the SM4 model for both databases and all three filter widths. This implies that post-reconstruction bounding has a substantial effect on the model performance; however, part of the improvement also originates from the direct use of the approximately reconstructed fields. This is in contrast to the SM4 model where the approximate reconstructions are used to develop an algbebraic model that entails further
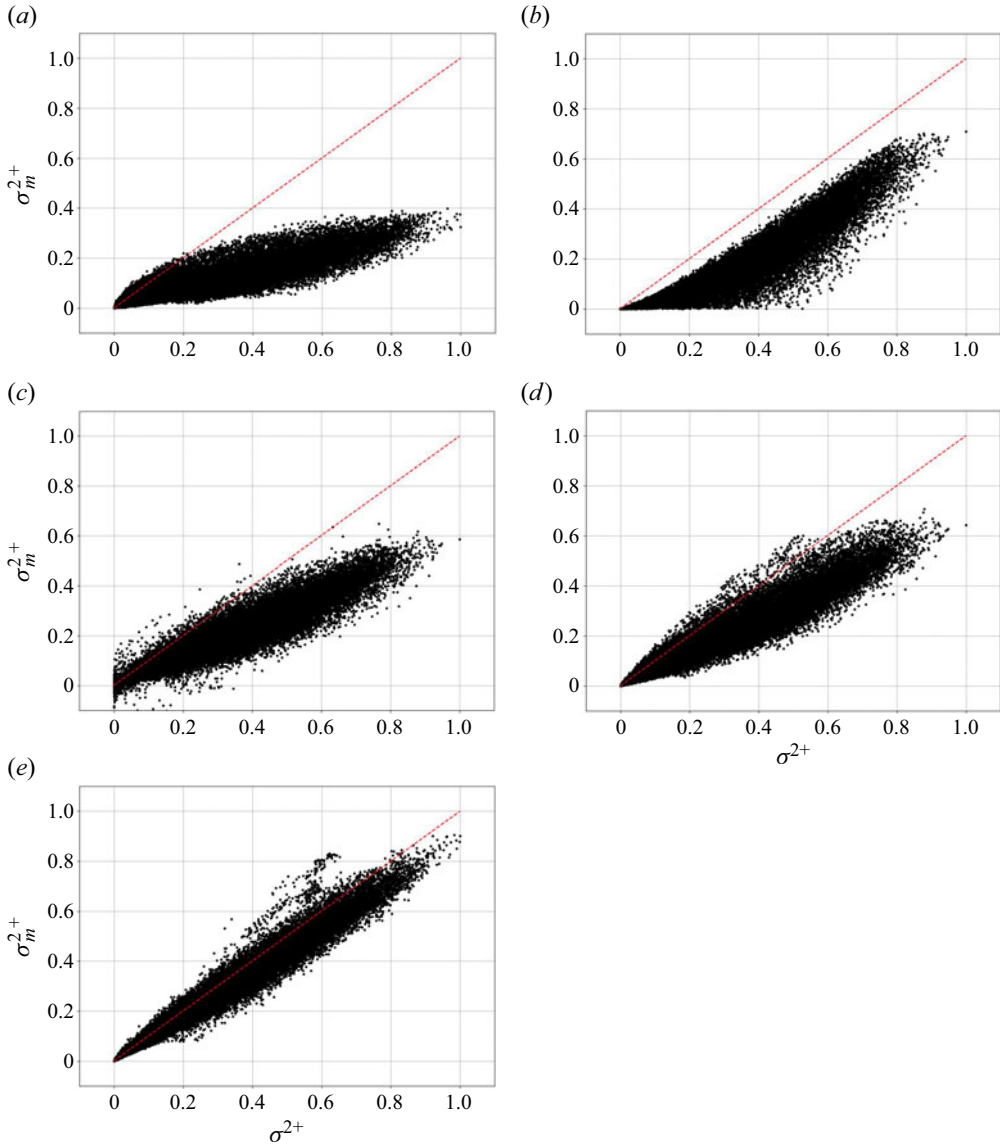
Figure 4. Instantaneous variance predictions of the static models against the reference variance for case V97 and $\Delta^+ = 3$. The predictions are normalised using the maximum reference variance. Results are shown for (*a*) SM2, (*b*) GR, (*c*) SM4, (*d*) AD4, (*e*) DEIF.

truncations of the filtering operations. Furthermore, we observe from figure 3 that the predictions of the AD4 model improve consistently over the entire range of $\tilde{c}$ values. Overall, the DEIF model has the best performance as evidenced by the lowest error, and the corresponding substantially improved conditional averages – figure 4(*e*) shows that this is a direct result of the much improved correlation with the reference variance. Between the two databases, DEIF performs better for the planar flame that exhibits larger-scale wrinkling. This is not surprising since the inverse filter was designed to correspond to $N = 5$ iterations of the van Cittert algorithm that is sufficient to recover the largest scales (smaller wavenumbers) for this flame. The V-flame on the other hand contains
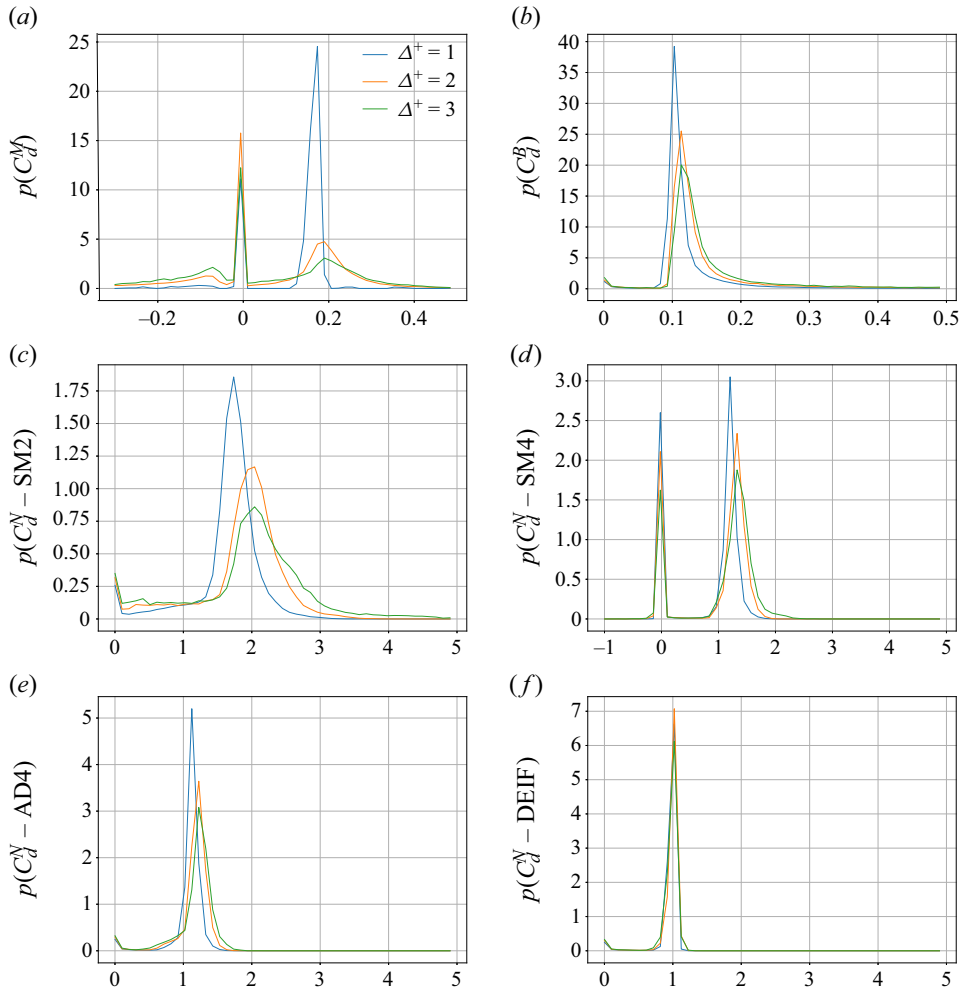
983 A47-26

Figure 5. Probability density functions of the different dynamic parameters: (*a*) C_d^M, (5.8); (*b*) C_d^B, (5.13); (*c*) C_d^N for the SM2 model, (5.21); (*d*) C_d^N for the SM4 model, (5.25); (*e*) C_d^N for the AD4 model, (5.30) and (*f*) C_d^N for the DEIF model, (5.30). The p.d.f.s are for case V97.

contributions from smaller scales and higher-order reconstruction is required to recover these, which leads to a slight under-prediction of the peak variance. Despite this, the predictions of the DEIF model are still substantially improved in comparison to the rest of the models.

Overall, these results combined serve to confirm the validity of the reconstruction-based modelling framework proposed in § 3, and one could employ higher-order reconstructions leading to further improvements. In the following section we examine whether the corresponding dynamic formulations of each of the above static models improve their predictions and to what extent.

	Δ^+	DSM2-N	DSM4-N	DGR-B	DAD4-N	DEIF-N
PB						
	1	2.364×10^{-5}	8.169×10^{-6}	1.288×10^{-5}	5.302×10^{-6}	6.474×10^{-7}
	2	9.662×10^{-5}	4.959×10^{-5}	8.050×10^{-5}	3.758×10^{-5}	9.080×10^{-6}
	3	1.993×10^{-4}	1.229×10^{-4}	1.763×10^{-4}	9.515×10^{-5}	2.707×10^{-5}
V97						
	1	3.364×10^{-5}	9.057×10^{-6}	1.244×10^{-5}	6.811×10^{-6}	1.678×10^{-6}
	2	1.928×10^{-4}	6.782×10^{-5}	1.024×10^{-4}	5.213×10^{-5}	1.483×10^{-5}
	3	5.599×10^{-4}	2.683×10^{-4}	3.744×10^{-4}	1.897×10^{-4}	6.247×10^{-5}

Table 9. Mean-squared errors obtained using (6.1) for each of the dynamic models.

6.3. *Comparison of C_d formulations*

Before quantifying the performance of the dynamic models, it is imperative to examine the distribution of each model's dynamic parameter. The p.d.f.s for each one are shown in figure 5 for case V97 (similar distributions were obtained for the planar flame). In accordance with the results obtained for a passive scalar by Balarac *et al.* (2008) but also for reacting scalars by Knudsen *et al.* (2010), C_d^M can become negative as evidenced by the finite non-zero probability for negative C_d^M values in figure 5(*a*). This leads to negative variance predictions that are not realisable. Perhaps more important however is that for increasing filter widths Δ, the probability of C_d^M becoming negative increases whereas the probability of becoming positive decreases. This trend, which is also in accordance with the results obtained by Balarac *et al.* (2008), implies that the predictions for this model deteriorate for increasing Δ. For these reasons, the variance predictions using this dynamic model were found to be inferior to the rest of the models. The formulation in (5.13) (C_d^B) on the other hand is always positive as expected, and more robust as it is less affected by variations in Δ. In the case of the DSM2-N model, the dynamic parameter is always positive by construction that is also reflected in the corresponding p.d.f. The distribution of C_d^N for the DSM4-N model on the other hand has some negative contributions owing to truncating the filtering operations to obtain the expression for T_m in (5.25). In the case of the DAD4-N model, C_d^N is also always positive by construction. It is also important to note that all four C_d^N formulations are much less sensitive to variations in filter width in comparison to the formulation for C_d^M. Also, since the base static models AD4 and DEIF already provide adequately good predictions of the variance, the corresponding p.d.f.s of their dynamic parameters approach a delta function centred around 1 in accordance with the limiting behaviour of the dynamic reconstruction models presented in § 5.

6.4. *Dynamic models*

Table 9 shows the errors for the five dynamic models. The conditional averages are shown in figure 6, and instantaneous predictions are shown in figure 7 for case V97 at $\Delta^+ = 3$. It is important to note at this point that all dynamic models employ a test filter $\hat{\Delta} = 2\Delta$, and regularisation of the dynamic parameter is conducted by averaging in the homogeneous directions in accordance with standard practice in the literature. Firstly, by comparing tables 8 and 9 we see that the dynamic procedure improves the predictions of the static models. This results in improved predictions of the peak variance as evidenced from the instantaneous predictions shown in figure 7 despite the generally
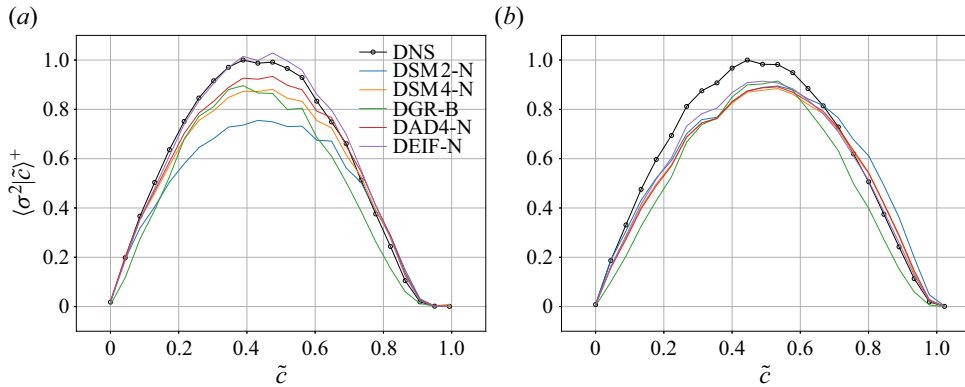
Figure 6. Conditionally averaged variance predictions of the dynamic models against the reference variance at $\Delta^+ = 3$ for (*a*) the planar flame and (*b*) the V-flame. Note that these are normalised using the maximum of the reference conditional variance. Results are shown for (*a*) PB $- \Delta^+ = 3$ and (*b*) V97 $- \Delta^+ = 3$.

more distributed predictions observed for the dynamic models. This increased scatter is the result of local variations in the dynamic parameter particularly in regions of intense heat release. In such regions, the standard averaging procedure in homogeneous directions may not be sufficient to smooth out any large variations. This issue has also been identified in past studies on turbulent premixed flames modelling, for instance, when calculating the dynamic Smagorinsky parameter (Klein, Kasten & Chakraborty 2015). An alternative averaging procedure that involves conditioning on $\tilde{c}$ may help to reduce the scatter as suggested by Klein *et al.* (2015). Nevertheless, the conditional averages are also improved for all $\tilde{c}$ values as we observe from figure 6. The dynamic procedure proposed in § 5 even improves the results of the static SM2 model that is the lowest-order reconstruction model ($O(\Delta^2)$), and which has the largest error of all the static models. In fact, for the largest filter width, the DSM2-N model compares favourably with the dynamic gradient model that is derived from an $O(\Delta^4)$ reconstruction approximation. These results serve to validate the dynamic modelling procedure that was reinterpreted as a two-level reconstruction-modelling approach in § 5. The DSM4-N model improves the results considerably over the DSM2-N model as a result of the higher-order Taylor expansion for the reconstructed fields. Some negative predictions do occur for reasons discussed in the previous section, however, the overall error is lower than the dynamic gradient model. Furthermore, from the instantaneous predictions in figure 7(*d*) we see that the overall correlation of the DSM4-N model is improved in comparison to the dynamic gradient model. The DAD4-N model on the other hand has the lowest error, highest correlation and best overall performance of all the algebraic models. The dynamic inverse filter model DEIF-N has the best overall performance and improves the predictions particularly in the leading edge ($\tilde{c} < 0.4$) of the flame surface as evidenced in figure 6(*b*). It is interesting to note that, for the V-flame, all models show similar responses when comparing their conditional averages, however, they all have substantially different errors and correlations with respect to the reference variance. This serves to illustrate that comparing conditional averages alone is insufficient for model comparison/evaluation.

7. Conclusions

A generalized modelling framework for the scalar variance in LES is presented. This new modelling framework is based on reconstruction of the primary variables with the
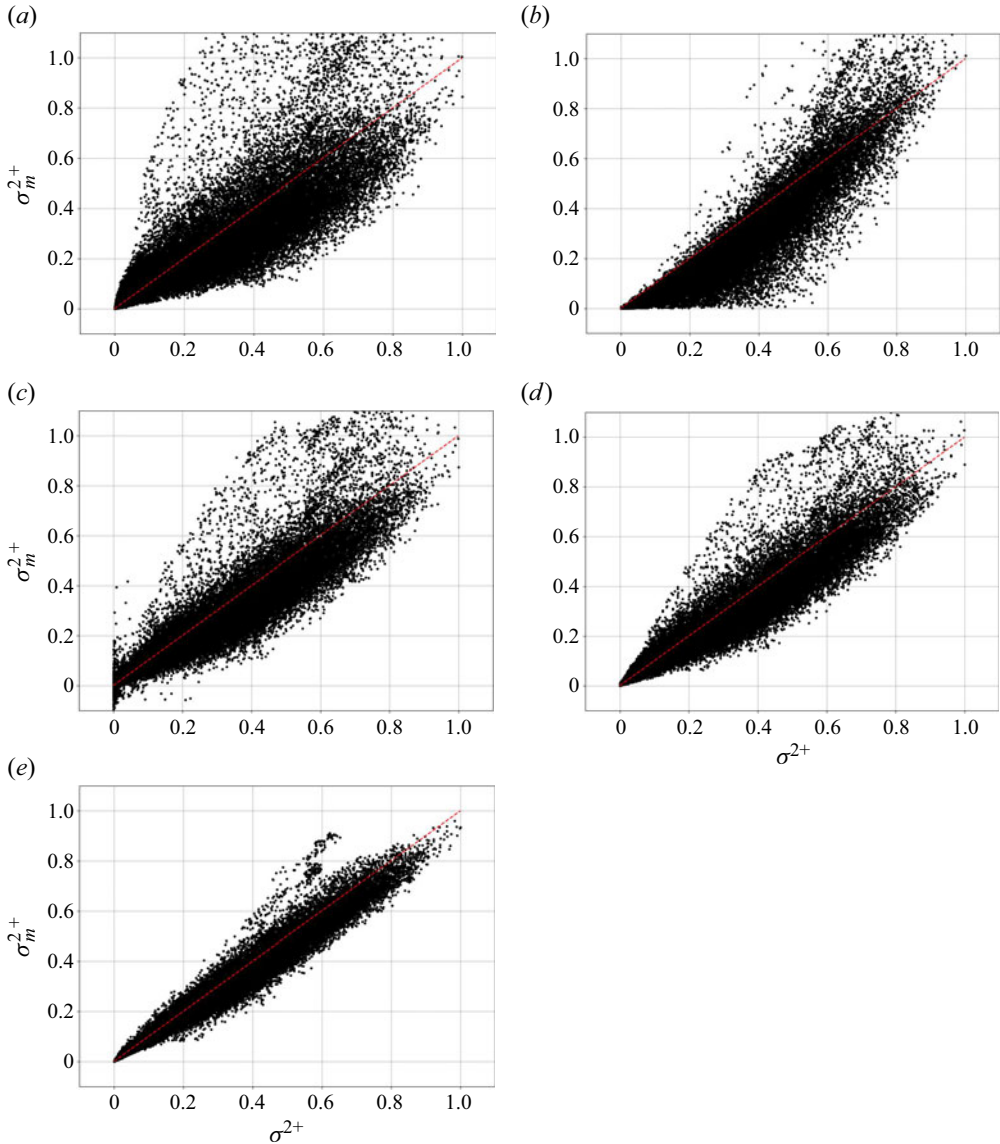
Figure 7. Instantaneous variance predictions of the dynamic models against the reference variance for case V97 and $\Delta^+ = 3$. The predictions are normalised using the maximum reference variance. Results are shown for (*a*) DSM2-N, (*b*) DGR-B, (*c*) SM4, (*d*) AD4, (*e*) DEIF.

degree of reconstruction determining the accuracy of the model. It is shown that the classic scale-similarity model of Cook & Riley (1994) but also the gradient model by Pierce & Moin (1998) are subsets of more general models derived using the proposed framework. Another novelty of the proposed framework is that the base static models are physically realisable by construction since the variance predictions are bounded, thus satisfying the relevant properties of the scalar variance.

The methodology for the development of dynamic models stems from a new interpretation of the classic scale-similarity assumption as a two-level reconstruction process whose aim is to correct the prediction of the base static model using information

983 A47-30

from the resolved scales. This involves a reconstruction step at the normal filter level Δ that serves to obtain a base static model, and a reconstruction step at the test-filter level $\hat{\Delta}$ that serves to obtain a model for the resolved variance. This naturally leads to an alternative interpretation of the model dynamic parameter C_d, which is intrinsic to the base model but also to the specific reconstruction operator used.

By employing approximate reconstruction operators obtained using truncated Taylor-series expansions, a range of static and dynamic algebraic models are developed. In addition, a novel and computationally efficient reconstruction operator based on the concept of optimised inverse explicit filters is used to develop a new high-order static and dynamic reconstruction model. All models are eventually tested *a priori* using high-fidelity DNS data of two turbulent premixed flames. The highest-order reconstruction models show a substantial improvement in comparison to the classic models serving to justify the proposed modelling framework. At the same time, their performance is consistent with variations in filter width despite the large differences in thermo-chemical properties and flow configuration between the two databases.

Even though approximate reconstruction operators were employed, the proposed modelling framework allows for any arbitrary higher-order approximate or iterative reconstruction operator to be used, therefore leading to higher-order variance models. In addition, the proposed dynamic procedure allows SGS effects to be incorporated in a base reconstruction model, thereby extending the capabilities of current reconstruction-based modelling methods. Furthermore, in contrast to classic modelling approaches, the modelling framework presented in this work is general. As such, it can be used to model a wide range of unresolved terms in the governing equations for LES, thereby providing a single, coherent and unified modelling framework for the simulation of turbulent flows.

Declaration of interests. The authors report no conflict of interest.

Author ORCIDs.
 Z. Nikolaou https://orcid.org/0000-0003-4201-2352.

Appendix A

Let $\phi(x, t) \in [0, 1]$ and $\tilde{G}(s; x, t) = G(s)\rho(x - s, t)/\bar{\rho}(x, t) \geq 0$ for all $s, x, t \in \mathbb{R}$ with the consistency condition $\int_{-\infty}^{\infty} \tilde{G}(s; x, t)\, \mathrm{d}s = 1$. We have

$$\tilde{\phi}(x, t) - 1 = \int_{-\infty}^{\infty} \tilde{G}(s; x, t)\, (\phi(x - s, t) - 1)\, \mathrm{d}s, \tag{A1}$$

where $(\phi(x - s, t) - 1) \in [-1, 0]$ and $\tilde{G}(s; x, t)(\phi(x - s, t) - 1) \leq 0$. As a result, $\tilde{\phi}(x, t) \leq 1$ for all $x, t \in \mathbb{R}$. Also, $\tilde{G}(s; x, t)\phi(x - s, t) \geq 0$, hence, $\tilde{\phi}(x, t) \geq 0$. Therefore, overall if $\phi \in [0, 1]$ then $\tilde{\phi} \in [0, 1]$ as well.

For non-positive filters, $\tilde{\phi}$ may not be bounded in $[0, 1]$ even if $\phi \in [0, 1]$. For such filters, there always exists by definition at least one region in space and time such that $\tilde{G}(s; x, t) < 0$ for all $s \in [a, b]$ where we will take $b > a$ without loss of generality.

In such a case we may define, for all $t \in \mathbb{R}$, the function

$$\phi(x - s, t) = \begin{cases} v \in [0, 1] \text{ constant}, & \text{for all } (x - s) \in [x - b, x - a], \\ 0, & \text{otherwise.} \end{cases} \tag{A2}$$

For the above distribution, the filtering integral reduces to

$$\tilde{\phi}(x, t) - 1 = \int_a^b \tilde{G}(s; x, t)(v - 1) \, \mathrm{d}s \tag{A3}$$

for all $(x - s) \in [x - b, x - a]$ and where $\tilde{G}(s; x, t)(v - 1) \geq 0$. Therefore, $\tilde{\phi}(x, t) \geq 1$ for all $(x - s) \in [x - b, x - a]$. Similarly, the lower bound is not satisfied either since for all $(x - s) \in [x - b, x - a]$ $\tilde{G}(s; x, t)v \leq 0$. In short, we have shown that, for non-positive filters and a bounded scalar $\phi \in [0, 1]$, there always exists a bounded distribution in $[0, 1]$ such that $\tilde{\phi}(x, t)$ is not bounded in $[0, 1]$.

REFERENCES

ADAMS, N. & STOLZ, S. 2002 A sub-grid scale deconvolution approach for shock-capturing. *J. Comput. Phys.* **178**, 391–426.

BALARAC, G., PITSCH, H. & RAMAN, V. 2008 Development of a dynamic model for the subfilter scalar variance using the concept of optimal estimators. *Phys. Fluids* **20**, 035114.

BARDINA, J., FERZINGER, J.H. & REYNOLDS, W.C. 1980 Improved subgrid scale models for large eddy simulation. In *AIAA 13th Fluid and Plasma Dynamics Conference*, pp. 80–1357.

BILGER, R.W., SAETRAN, L.R. & KRISHNAMOORTHY, L.V. 1991 Reaction in a scalar mixing layer. *J. Fluid Mech.* **233**, 211–242.

BOGUSLAWSKI, A., WAWRZAK, K., PALUSZEWSKA, A. & GEURTS, B.J. 2021 Deconvolution of induced spatial discretization filters subgrid modeling in LES: application to two-dimensional turbulence. *J. Phys.* **2090**, 1–10.

BORGHI, R. 1988 Turbulent combustion modelling. *Prog. Energy Combust. Sci.* **14**, 245–292.

BRAY, K.N.C. 1996 The challenge of turbulent combustion. *Symp. (Intl) Combust.* **26**, 1–26.

BRAY, K.N.C., LIBBY, P.A. & MOSS, J.B. 1985 Unified modeling approach for premixed turbulent combustion. Part I. General formulation. *Combust. Flame* **61**, 87–102.

BRAY, K.N.C. & MOSS, J.B. 1977 A unified statistical model of the premixed turbulent flame. *Acta Astronaut.* **4**, 291–319.

BULL, J.R. & JAMESON, A. 2016 Explicit filtering and exact reconstruction of the sub-filter stresses in large eddy simulation. *J. Comput. Phys.* **306**, 117–136.

CANT, R.S. 2012 SENGA2 User Guide, CUED A-THERMO-TR67.

CARATI, D., WINCKELMANS, G.S. & JEANMART, H. 2001 On the modelling of the subgrid-scale and filtered-scale stress tensors in large-eddy simulation. *J. Fluid Mech.* **441**, 119–138.

VAN CITTERT, P.H. 1931 Zum Einfluss der Spaltbreite auf die Intensitatsverteilung in Spektrallinien. II. *Z. Phys.* **69**, 298–308.

CLARK, R.A., FERZINGER, H. & REYNOLDS, W.C. 1979 Evaluation of subgrid-scale models using an accurately simulated turbulent flow. *J. Fluid Mech.* **91**, 1–16.

COOK, A. & RILEY, C. 1994 A subgrid model for equilibrium chemistry in turbulent flows. *Phys. Fluids* **6**, 2868–2870.

DATTA, A., MATHEW, J. & HEMCHANDRA, S. 2022 The explicit filtering method for large eddy simulations of a turbulent premixed flame. *Combust. Flame* **237**, 111862.

DOMINGO, P., NIKOLAOU, Z., SELTZ, A. & VERVISCH, L. 2020 *From Discrete and Iterative Deconvolution Operators to Machine Learning for Premixed Turbulent Combustion Modeling*, pp. 215–232. Springer.

DOMINGO, P. & VERVISCH, L. 2015 Large eddy simulation of premixed turbulent combustion using approximate deconvolution and explicit flame filtering. *Proc. Combust. Inst.* **35**, 1359–1357.

DOMINGO, P. & VERVISCH, L. 2017 DNS and approximate deconvolution as a tool to analyse one-dimensional filtered flame sub-grid scale modelling. *Combust. Flame* **177**, 109–122.

DOMINGO, P., VERVISCH, L. & VEYNANTE, D. 2008 Large-eddy simulation of a lifted methane-air jet flame in a vitiated coflow. *Combust. Flame* **152** (3), 415–432.

DOPAZO, C. 1979 Relaxation of initial probability density functions in the turbulent convection of scalar fields. *Phys. Fluids* **22** (1), 20–30.

FOX, R.O. 2003 *Computational Models for Turbulent Reacting Flows*. Cambridge University Press.

FUKAMI, K., FUKAGATA, K. & TAIRA, K. 2020 Machine-learning-based spatio-temporal super resolution reconstruction of turbulent flows. *J. Fluid Mech.* **909**, A9.

GERMANO, M., PIOMELLI, U., MOIN, P. & CABOT, W.H. 1991 A dynamic subgrid-scale eddy viscosity model. *Phys. Fluids* **4**, 1760–1765.

GHOSAL, S., LUND, T.S., MOIN, P. & AKSELVOLL, K. 1995 A dynamic localization model for large eddy-simulation of turbulent flows. *J. Fluid Mech.* **286**, 229–255.

GIRIMAJI, S.S. & ZHOU, Y. 1995 Analysis and modeling of subgrid scalar mixing using numerical data. *Phys. Fluids* **8**, 1224–1236.

GULLBRAND, J. & CHOW, F.K. 2003 The effect of numerical errors and turbulence models in large-eddy simulations of channel flow, with and without explicit filtering. *J. Fluid Mech.* **495**, 323–341.

GUTHEIL, E., BALAKRISHNAN, G. & WILLIAMS, F.A. 1993 Structure and extinction of hydrogen-air diffusion flames. In *Reduced Kinetic Mechanisms for Applications in Combustion Systems* (ed. N. Peters & B. Rogg), Lecture Notes in Physics. Springer.

JIMENEZ, C., DUCROS, F., CUENOT, B. & BEDAT, B. 2001 Subgrid scale variance and dissipation of a scalar field in large eddy simulations. *Phys. Fluids* **13**, 1748–1754.

JIMENEZ, J., LINAN, A., ROGERS, M.M. & HIGUERA, F.J. 1997 A priori testing of subgrid models for chemically reacting non-premixed turbulent shear flows. *J. Fluid Mech.* **349**, 149–171.

JONES, W.P. & LAUNDER, B.E. 1972 The prediction of laminarization with a two-equation model of turbulence. *J. Heat Mass Transfer* **15**, 301–314.

KEIL, F.B., KLEIN, M. & CHAKRABORTY, N. 2021 Sub-grid reaction progress variable variance closure in turbulent premixed flames. *Flow Turbul. Combust.* **106**, 1195–1212.

KIM, H., KIM, J., WON, S. & LEE, C. 2021 Unsupervised deep learning for super-resolution reconstruction of turbulence. *J. Fluid Mech.* **910**, A29.

KLEIN, M., KASTEN, C. & CHAKRABORTY, N. 2015 A-priori direct numerical simulation assessment of sub-grid scale stress tensor closures for turbulent premixed combustion. *Comput. Fluids* **122**, 1–11.

KNUDSEN, E., KIM, S.H. & PITSCH, H. 2010 An analysis of premixed flamelet models for large eddy simulation of turbulent combustion. *Phys. Fluids* **22**, 115109.

KOLLA, H., ROGERSON, J.W., CHAKRABORTY, N. & SWAMINATHAN, N. 2009 Scalar dissipation rate modelling and its validation. *Combust. Sci. Technol.* **181**, 518–535.

LECOCQ, G., RICHARD, S., COLIN, O. & VERVISCH, L. 2011 Hybrid presumed pdf and flame surface density approach for large-eddy simulation of premixed turbulent combustion. Part 1. Formalism and simulations of a quasi-steady burner. *Combust. Flame* **158** (6), 1201–1214.

LELE, S.K. 1992 Compact finite-difference schemes with spectral-like resolution. *J. Comput. Phys.* **103**, 16–42.

LEONARD, A. 1997 Large-eddy simulation of chaotic convection and beyond. In *AIAA Meeting Papers on Disc, January 1997*, A9715284, 97-0204.

LILLY, D.K. 1992 A proposed modification of the germano subgrid-scale closure method. *Phys. Fluids* **4**, 633–635.

LIU, S., MENEVEAU, C. & KATZ, J. 1994 On the properties of similarity subgrid-scale models as deduced from measurements in a turbulent jet. *J. Fluid Mech.* **275**, 83–119.

LOCKWOOD, F.C. & NAGUIB, A.S. 1975 The prediction of the fluctuations in the properties of free, round-jet, turbulent, diffusion flames. *Combust. Flame* **24**, 109–124.

LOGINOV, M.A., ADAMS, N.A. & ZHELTOVODOV, A.A. 2006 Large-eddy simulation of shock-wave/turbulent-boundary-layer interaction. *J. Fluid Mech.* **565**, 135–169.

MATHEW, J. 2002 Large eddy simulation of a premixed flame with approximate deconvolution modelling. *Proc. Combust. Inst.* **29**, 1995–2000.

MATHEW, J., FOYSI, H. & FRIEDRICH, R. 2006 A new approach to LES based on explicit filtering. *Intl J. Heat Fluid FLow* **27**, 594–602.

MATHEW, J., LECHNER, R., FOYSI, H., SESTERHENN, J. & FRIEDRICH, R. 2003 An explicit filtering method for large eddy simulation of compressible flows. *Phys. Fluids* **15**, 2279–2289.

MAULIK, R. & SAN, O. 2017 A neural network approach for the blind deconvolution of turbulent flows. *J. Fluid Mech.* **831**, 151–181.

MESQUITA, C.C., MASTORAKOS, E. & ZEDDA, M. 2023 LES-CMC of high-altitude relight in an RQL aeronautical combustor. *Proc. Combust. Inst.* **39** (4), 4811–4820.

MINAMOTO, Y., FUKUSHIMA, N., TANAHASHI, M., MIYAUCHI, T. & DUNSTAN, T. 2011 Effect of flow geometry on turbulence-scalar interaction in premixed flames. *Phys. Fluids* **23**, 125107.

Moss, J.-B. & Bray, K.N.C. 1977 A unified statistical model of the premixed turbulent flame. *Acta Astronaut.* **4**, 291–319.

Mukhopadhyay, S., van Oijen, J.A. & de Goey, L.P.H. 2015 A comparative study of presumed PDFs for premixed turbulent combustion modeling based on progress variable and its variance. *Fuel* **159**, 728–740.

Nambully, S., Domingo, P., Moureau, V. & Vervisch, L. 2014 A filtered-laminar-flame PDF sub-grid scale closure for LES of premixed turbulent flames. Part I. Formalism and application to a bluff-body burner with differential diffusion. *Combust. Flame* **161** (7), 1756–1774.

Nikolaou, Z., Minamoto, Y. & Vervisch, L. 2019 Unresolved stress tensor modeling in turbulent premixed V-flames using iterative deconvolution: an a priori assessment. *Phys. Rev. Fluids* **4**, 063202.

Nikolaou, Z., Vervisch, L. & Domingo, P. 2022 Criteria to switch from tabulation to neural networks in computational combustion. *Combust. Flame* **246**, 112425.

Nikolaou, Z., Vervisch, L. & Domingo, P. 2023 An optimisation framework for the development of explicit discrete forward and inverse filters. *Comput. Fluids* **255**, 105840.

Nikolaou, Z.M. & Swaminathan, N. 2013 A 5-step reduced mechanism for combustion of $CO/H_2/H_2O/CH_4/CO_2$ mixtures with low hydrogen/methane and high H_2O content. *Combust. Flame* **160**, 56–75.

Nikolaou, Z.M. & Swaminathan, N. 2015 Direct numerical simulation of complex fuel combustion with detailed chemistry: physical insight and mean reaction rate modelling. *Combust. Sci. Technol.* **187**, 1759–1789.

Nikolaou, Z.M. & Vervisch, L. 2018 A priori assessment of an iterative deconvolution method for LES sub-grid scale variance modelling. *Flow Turbul. Combust.* **101**, 33–53.

Nikolaou, Z.M., Vervisch, L. & Cant, R.S. 2018 Scalar flux modelling in turbulent flames using iterative deconvolution. *Phys. Rev. Fluids* **3**, 043201.

Pantano, C., Sarkar, R. & Williams, F.A. 2003 Mixing of a conserved scalar in a turbulent reacting shear layer. *J. Fluid Mech.* **481**, 291–328.

Pera, C., Reveillon, J., Vervisch, L. & Domingo, P. 2006 Modeling subgrid scale mixture fraction variance in les of evaporating spray. *Combust. Flame* **146**, 635–648.

Peters, N. 2000 *Turbulent Combustion*. Cambridge University Press.

Pierce, C.D. & Moin, P. 1998 A dynamic model for subgrid-scale variance and dissipation rate of a conserved scalar. *Phys. Fluids* **10**, 3041–3044.

Pierce, C.D. & Moin, P. 2004 Progress-variable approach for large-eddy simulation of non-premixed turbulent combustion. *J. Fluid Mech.* **504**, 73–97.

Poinsot, T. & Lele, S. 1992 Boundary conditions for direct simulations of compressible viscous flows. *J. Comput. Phys.* **101**, 104–129.

Schlatter, P., Stolz, S. & Kleiser, L. 2004 LES of transitional flows using the approximate deconvolution model. *Intl J. Heat Fluid Flow* **25**, 549–558.

Smagorinsky, J. 1963 General circulation experiments with the primitive equations. *Mon. Weath. Rev.* **91**, 99–164.

Stolz, S. & Adams, N. 1999 An approximate deconvolution procedure for large-eddy simulation. *Phys. Fluids* **11**, 1699–1701.

Stolz, S. & Adams, N. 2001 An approximate deconvolution model for large-eddy simulation with application to incompressible wall-bounded flows. *Phys. Fluids* **13**, 997–1015.

Sutherland, J.C. & Kennedy, C.A. 2003 Improved boundary conditions for viscous, reacting compressible flows. *J. Comput. Phys.* **191**, 502–524.

Thompson, K.W. 1987 Time dependent boundary conditions for hyperbolic systems. *J. Comput. Phys.* **68**, 1–24.

Veynante, D. & Vervisch, L. 2002 Turbulent combustion modeling. *Prog Energy Combust. Sci.* **28**, 193–266.

Vreman, A.W., Albrecht, B.A., van Oijen, J.A., de Goey, L.P.H. & Bastiaans, R.J.M. 2008 Premixed and nonpremixed generated manifolds in large-eddy simulation of Sandia flame D and F. *Combust. Flame* **153**, 394–416.

Vreman, A.W., Bastiaans, R.J.M. & Geurts, B.J. 2009*a* A similarity subgrid model for premixed turbulent combustion. *Flow Turbul. Combust.* **82**, 233–248.

Vreman, A.W., van Oijen, J.A., de Goey, L.P.H. & Bastiaans, R.J.M. 2009*b* Subgrid scale modeling in large-eddy simulation of turbulent combustion using premixed flamelet chemistry. *Flow Turbul. Combust.* **82**, 511–535.

Wang, Q. & Ihme, M. 2017 Regularized deconvolution method for turbulent combustion modelling. *Combust. Flame* **176**, 125–142.

Wang, Q. & Ihme, M. 2019 A regularised deconvolution method for turbulent closure modelling in implicitly filtered large-eddy simulation. *Combust. Flame* **204**, 341–355.